Full Spectrum Utilization for High-Efficiency Solar Energy Conversion

by

David M. Bierman

S.M. Mechanical Engineering, Massachusetts Institute of Technology, 2014
B.S. Mechanical Engineering, University of Wisconsin – Madison, 2012

Submitted to the Department of Mechanical Engineering
in partial fulfillment of the requirements for the degree of

Doctor of Philosophy in Mechanical Engineering

at the

MASSACHUSETTS INSTITUTE OF TECHNOLOGY
September 2017

Signature redacted

Signature of Author: .....

Department of Mechanical Engineering
August 8, 2017

Signature redacted

Certified by: .....

Evelyn N. Wang
Associate Professor of Mechanical Engineering
Thesis Supervisor

Signature redacted

Accepted by: .....

Rohan Abeyarante
Chairman, Department Committee on Graduate Theses

Full Spectrum Utilization for High-Efficiency Solar Energy Conversion

by

David M. Bierman

Submitted to the Department of Mechanical Engineering on August 8th, 2017,
in Partial Fulfillment of the Requirements for the Degree of Doctor of Philosophy

Abstract

Today, two dominant strategies for solar energy harvesting exist: solar thermal and photovoltaic. Solar thermal energy harvesting offers the distinct ability to both utilize the full solar spectrum and provide dispatchable electrical power to the grid. By contrast, the generation of power via the photovoltaic effect can reduce the complexity of a system by eliminating moving parts. Conversion strategies which use both thermal and photovoltaic principles capitalize on the advantages of each. This thesis explores the potential of these technologies through both experimental and theoretical device-level studies.

First, we explored solar thermophotovoltaic devices (STPVs) which convert broadband sunlight to narrow-band thermal radiation tuned for a photovoltaic cell. We demonstrated the highest STPV efficiency to date through the suppression of 80% of sub-bandgap blackbody radiation by pairing a one-dimensional photonic-crystal selective emitter with a tandem plasma-interference optical filter. We measured a solar-to-electrical conversion rate of 6.8%, exceeding the performance of the photovoltaic cell alone. Additionally, we show experimentally that STPVs can reduce the heat generation rates in the photovoltaic cell by a factor of two for the same power density.

Next, we explored the use of spectral splitting as a different strategy to use both thermal and photovoltaic technologies. A model of an ideal solar spectral-splitting converter was developed to determine the conversion efficiency limit as well as the corresponding optimum spectral bandwidth of sunlight which should illuminate the photovoltaic cell. This bandwidth was also obtained analytically through an entropy minimization scheme and matches well with our model. We show that the maximum efficiency of the system occurs when it minimizes the spectral entropy generation.

Beyond solar energy harvesting, we investigated the radiation dynamics of vanadium dioxide (VO_2), which is of interest because of the abrupt decline of emittance at the insulator-metal transition at ~340 K. Negative differential emission is exploited to demonstrate thermal runaway of this system for the first time. These results are used to validate a radiation heat transfer model which explores the limiting behavior of a VO_2 material set.

These studies together show the power of controlling radiation heat transfer, both through spectral and temperature-dependent optical properties. By studying the effects of these properties at the device level, we elucidate the potential for many emerging technologies.

Committee:

Professor Evelyn N. Wang (Thesis Advisor/Chair), Department of Mechanical Engineering
Professor Gang Chen, Department of Mechanical Engineering
Professor Marin Soljačić, Department of Physics

Acknowledgements

The work described in this thesis is highly collaborative. As a part of the Rohsenow Kendall Heat Transfer Laboratory and the Solid State Solar Thermal Energy Conversion (S3TEC) Center, I had the privilege of being surrounded by highly gifted scientists and engineers. Specifically, I'd like to thank the following individuals for their direct contribution to this thesis: Walker Chan (Chapter 2), Colin Kelsall (Chapter 3), Mikhail Kats (Chapter 4), Bikram Bhatia, Ivan Celanovic, Marin Soljacic, Svetlana Boriskina, Bolin Liao, Lee Weinstein, and Professor Gang Chen. Thanks to Duanhui Lu and Professor Carl Thompson for training and access to their CVD growth facilities; to Tim McClure at the CMSE for FTIR spectroscopy; to Kurt Broderick and other technical staff at the MTL. I'm appreciative of the funding support from S3TEC and the MIT Energy Initiative.

I am unable to fully express my gratitude towards my thesis advisor, Professor Evelyn N. Wang. I feel fortunate to have worked with a human who embodies all the proper characteristics of a leader. From our first conversation, I was certain that I would not be able to find a better advisor for myself. Her style of academic mentorship is unique through a simultaneously involved, yet hands-off approach to her students' research projects. She is ambitious in her demands, but reasonable in her guidance. She inspires those around her to not just work hard, but to do so with integrity, care, and perspective. It has been a pleasure working with her.

I had another thesis advisor while earning my doctoral degree -- Professor Andrej Lenert. As a doctoral student in the Device Research Lab, he cultivated my experimental and analytical skills from the time that I arrived at MIT. He departed two years later to the University of Michigan – Ann Arbor where he currently holds a professorship in the department of Chemical Engineering. Professor Lenert has closely guided me through all the work presented in this thesis. Together, we developed concepts in solar thermophotovoltaics and had fun doing it. He has always made himself available to me (even when I am positive he did not feel like). His brilliance is inspiring, and I'm eternally glad that I had the opportunity to learn so much from him. Andrej has made me a better person and I look forward to what the future has in store for our future collaborations.

Thank you to members of the Device Research Lab. The support from my labmates, both technical and otherwise, is a large contributor to this thesis. Special thanks to Daniel Preston, Jeremey Cho, Heena Mutha, Yangying Zhu, Sungwoo Yang, Dion Antao, Zhengmao Lu, Hyunho Kim, Arny Leroy, Elise Strobach, Alexandra Cabral, and others.

Thank you to my wonderful friends at MIT; to my roommates, Tim Murray, Jose Sandt, and Levi Lentz; to Chris Bachman, Maia Kostlan, Buddy Bachman, Sadie Bachman, Tyler Wortman, Daniel Preston, Adam Weiner; to my best friend Maria Luckyanova for her warmth, care, and love. These incredible people all helped me build a family at MIT.

A special thank you to my family. Their support and encouragement continue to enable my own personal success.

Table of Contents

List of Figures

Chapter 1

1. Introduction

1.1 MOTIVATION

The earth receives approximately 2.5 kWh of solar energy per square meter each day. For context, humans will consume approximately 4 Wh per square meter of the non-arable land on earth by 2040[1]. The three order of magnitude discrepancy between the solar resource and our energy demands should be regarded as a source of optimism. Today, there are two conventional methods of harnessing this energy: Solar thermal and solar photovoltaic. Recently, the widespread adoption of solar photovoltaic technologies has led to huge installations which now make up ~2% of the global electricity generation[2] and 99% of solar power generation[3].These devices, however, are only capable of generating electrical power while the sun is shining. This inability to provide continuous power without the use of prohibitively expensive electrical batteries will ultimately limit the penetration of solar energy utilization in the electricity resource portfolio of the future[4].

Alternatively, solar thermal energy conversion offers the distinct ability to provide continuous power to the grid without electrical batteries. Furthermore, technologies based on thermal energy conversion can harness the entire solar spectrum and theoretically achieve very high efficiencies. Large-scale power conversion based on solar thermal technologies is still relatively limited with only a few plants currently operating worldwide and few investments in new projects. As the temperature of these systems increases, so do both the opportunity for widespread thermal energy storage [5] and the efficiency of the converter[6]. Thus, it is important to look towards new classes of converters that can operate at high temperatures (>1000 °C).

In doing so, the elegance of the photovoltaic effect should not be discounted. These optoelectronic devices may be used for their ability to convert photons of a given wavelength to electricity without the need for moving parts. Conversion strategies which utilize both thermal and photovoltaic principles capitalize on the advantages of each. This thesis explores the potential of these technologies through both experimental and theoretical device-level studies.

1.2 BACKGROUND: SOLAR THERMAL

Solar thermal conversion relies on high absorption of typically concentrated sunlight and high suppression of parasitic heat loss to deliver thermal energy to a heat engine. In the most general case, the efficiency of this system can be represented by the product of the photo-thermal (PT) efficiency and the thermal-to-electric or heat engine (HE) efficiency:

$$\eta_{system} = \eta_{PT}\eta_{HE} \tag{1}$$

Among other things, these two efficiencies will rely heavily on the system temperature. For traditional solar thermal engineering, the efficiency of the photo-thermal conversion can be expressed as:

$$\eta_{PT} = \alpha - \frac{\epsilon\sigma(T_h^4 - T_{amb}^4) + h(T_h - T_{amb})}{\eta_c C G_s} \tag{2}$$

where α is the solar-weighted absorptance, ϵ is the thermally-weighted emittance, σ is the Stefan-Boltzmann constant, T_h is the absorber temperature, T_{amb} is the ambient temperature, h is the generalized heat transfer coefficient, η_c is the concentrating optics efficiency, C is the optical concentration, and G_s is the solar constant. Equation 2 shows the importance of high absorptance, low thermal emittance, low heat transfer coefficients, high optical efficiency, and high optical concentration. For medium temperature applications, solar engineers utilize spectral selectivity[7]–[9] (high absorptance in solar wavelengths with simultaneous low emittance in thermal wavelengths) to achieve high photo-thermal efficiencies. However, if high temperature is desired, equation 2 illustrates that high optical concentrations must be implemented for efficient energy conversion[10], [11]. Photo-thermal efficiencies can be as high as 95% depending on the specific operating condition of the heat engine.

Today, commercial solar thermal plants which generate power utilize traditional mechanical heat engines[12]. These converters are governed by conventional thermodynamics[13]. However, it has

been proposed that high temperature solar thermal plants of the future will take advantage of more advanced solid-state technologies including thermophotovoltaics[14], thermoelectrics[15], thermionics[16] and others. These conversion strategies each have their own limitations and dependence on operating temperature. One technology that is developed and explored in great detail in this thesis is the thermophotovoltaic converter which has a theoretical limit of ~80% and a more practical limit of ~60%. The rapid development of this class of solid-state converters could result in a drastically more straightforward solar energy harvesting strategy that may lead to inexpensive and widespread adoption.

1.3 BACKGROUND: PHOTOVOLTAICS AND SPECTRAL MODIFICATION

Photovoltaic devices convert radiation into electricity through the direct generation and extraction of electron-hole pairs within a semi-conductor. The photovoltaic cell is a frequency dependent device, which is illustrated in Figure 1. When illuminated by sunlight, the fixed solar spectrum and the fixed bandgap define a physical limit which is governed by the amount of energy above and below the bandgap of the semiconductor. This limit is known as the Shockley-Queisser limit[17], [18] and limits solar photovoltaic conversion to ~30% with unconcentrated sunlight.

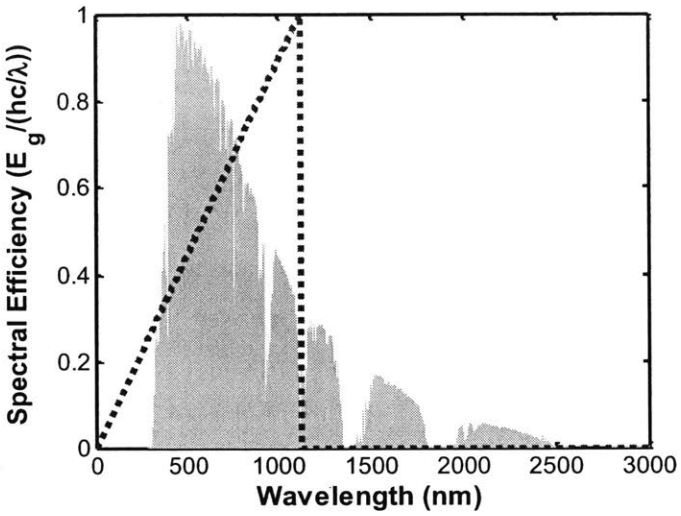

Figure 1: Frequency dependence of a photovoltaic cell. Below the bandgap (~1100 nm in this example), photon energies cannot be utilized. Above the bandgap, the portion of the photon energy that can be extracted is proportional to the wavelength.

The broad nature of sunlight is ultimately what limits the solar photovoltaic process. Depending on the semi-conductor material, particular wavelengths can be converted to electricity with high efficiency. Thus, there has been significant interest in narrowing the illumination spectrum that reaches the photovoltaic cell. While it is possible to do this by increasing the number of bandgaps with multi-junction cells[19], [20] or the generated charge carriers per absorbed photon with multi-exciton generation[21], altering the photon spectrum that illuminates a single junction photovoltaic cell has been of significant interest[22] to exceed the Shockley-Queisser limit.

Photon down-/up-conversion has been explored by exploiting photon energies additively to modify the incident spectrum using a three photon process, *i.e.*, using a high energy photon to create two lower energy photons each above the bandgap and thus two excited charge carriers[23]-[24] or two sub-bandgap photons to create a higher energy photon above E_g and thus a single charge carrier[25]. While these schemes promise to enhance power generation rates from sunlight by taking advantage of energy transitions within various luminescent materials[25]–[28], device level proof-of-concept down-/up-converter system efficiencies have yet to be reported[29]. This is mainly due to the parasitic self-absorption of the converted photons[30], the strong reflection

induced when such a converter is present[28] and the difficulty of fabrication of a quantum converter integrated within a solar cell architecture[23].

Similarly, photon shifting of a high energy photon into a lower one that is more efficiently converted by the photovoltaic cell [31] has received significant interest due to its potential performance enhancements for cells exhibiting poor quantum response at high energies. Despite this technology's ability to exceed the Shockley-Queisser limit, a variety of approaches for spectral-shifting have been explored to enhance the efficiency of photovoltaic conversion such as with quantum dots[31], [32], luminescent films[33], defect exploitation[34]. As with photon conversion, photon shifting strategies have suffered from high parasitic absorption within the host material and strong induced reflection above the solar cell based on the high refractive index mismatch.

1.4 THESIS OBJECTIVES AND OUTLINE

In this thesis, we address these common problems of spectral manipulation by investigating two promising technologies which limit the illumination of a photovoltaic cell to a narrow spectral range. More broadly, the studies presented together show the power of engineering radiation heat transfer, both through spectral and temperature-dependent optical properties. By studying the effects of these properties at the device level, we elucidate the potential for many important applications in emerging energy technologies.

In chapter 1, the motivation for hybridizing solar thermal and photovoltaic principles was presented. The basic considerations for solar thermal engineering as well as a literature review for spectral manipulation for increasing photovoltaic efficiency was discussed.

In chapter 2, a solar thermophotovoltaic device that demonstrates broadband solar absorption and near-ideal step function thermal emission is presented. This device holds the current world record for solar-to-electrical conversion at 6.8%. Implications for exceeding the Shockley-Queisser limit are discussed.

In chapter 3, the gap between the theoretical limits and the experimental demonstration is addressed. A detailed analysis is presented which accounts for the >90% power loss in the system. This study elucidates the aspects of a solar thermophotovoltaic that need further development to unlock the full potential of the technology.

In chapter 4, a converter that relies on separating sunlight based on wavelength is discussed. The theoretical limits of this hybrid thermal / photovoltaic system as well as the underlying thermodynamics are explored. A general framework for optimizing hybrid converters is presented.

In chapter 5, we look beyond solar energy harvesting and look at the radiation heat transfer dynamics of vanadium oxide (VO_2). By exploiting the negative differential emission of this material, we demonstrated thermal runaway in this system for the first time.

Chapter 2

2. Enhanced Photovoltaic Energy Conversion Using Thermally-based Spectral Shaping

2.1 INTRODUCTION

Since a photovoltaic device (PV) can only generate electrical power when illuminated by photons with higher energy than the electronic bandgap of the material ($E_{photon} > E_g$), the broad spectral nature of sunlight gives rise to the well-known Shockley-Queisser efficiency limit[17]. One method of getting beyond this limit is to alter the incident photon spectrum via a spectral converter. Luminescence is a common strategy to achieve this photon conversion[2,][24] and demonstrations have successfully taken advantage of energy transitions within various materials[4–7]. Device level system efficiencies have not yet been reported[8], however, due to the substantial challenges associated with parasitic self-absorption[9], strong reflections induced at the spectral converter/vacuum interface[7], and fabrication of an integrated quantum converter within a solar cell architecture[2].

To bypass these challenges and enable greater functionality, we have been investigating solar thermophotovoltaic converters (STPVs, Figure 1a). In this approach, the absorption of sunlight and subsequent re-emission of electromagnetic radiation is achieved via tuned thermal emission from nanophotonic structures. The entire incident photon spectrum is harnessed through a broadband, index-matched thermalization process by a high temperature (>1000°C) absorber. This induces thermal excitations within the emitter structure, creating a thermal emission spectrum which generates free electrons that are localized to the conduction band edge in the PV (Figure 1b). When coupled with strong suppression of sub-bandgap photon emission, high efficiency is attained by means of the spectral shift, while absorbed photon thermalization in the PV cell is reduced and excessive heat generation rates can be eliminated. This effect could enable passive cooling of the PV despite the device typically being under high solar concentration (>100 suns).

Additionally, as a thermal engine, STPVs allow for the integration of auxiliary heating[10] and thermal energy storage[11] for continuous operation, the most appealing feature of STPVs relative to other spectral converters. Thus, STPVs have been a particularly attractive technology since they address the common power generation concerns of efficiency, waste heat management, and dispatchability.

Recently, a variety of photonic designs exhibiting spectral control of either reflection[38] or high temperature thermal emission[39]–[42] have been proposed, fabricated, and integrated into STPVs[7], [10], [43], [44] for proof-of-concept demonstrations. The efficiency of these devices is typically at or below about 3%. Note that Shimizu *et al.*[44], [45]reported an efficiency estimate of ~8% for a different geometric configuration of the demonstrated material set. Their actual experimental efficiency is estimated to be ~0.5% given their reported view factors. While the results are promising, a direct comparison of these devices with their underlying PV is lacking and therefore enhanced performance due to an altered spectrum has not been shown. Here, we successfully pair a tandem plasma-interference optical filter with a one-dimensional Si/SiO_2 photonic crystal thermal emitter to show spectral enhancement in a STPV device. Our theoretical and experimental results indicate that the addition of this three-component (absorber-emitter-filter) thermally-based spectral converter can exceed the efficiency and reduce waste heat generation by a factor of two while maintaining the output power density of the underlying PV. Furthermore, we report STPV device conversion rates of 6.8%, ~2x greater than previously measured solar-to-electrical STPV efficiencies. This work is an important step towards realizing a solar driven power generator capable of producing electricity with a single junction PV cell at efficiencies exceeding the Shockley-Queisser limit.

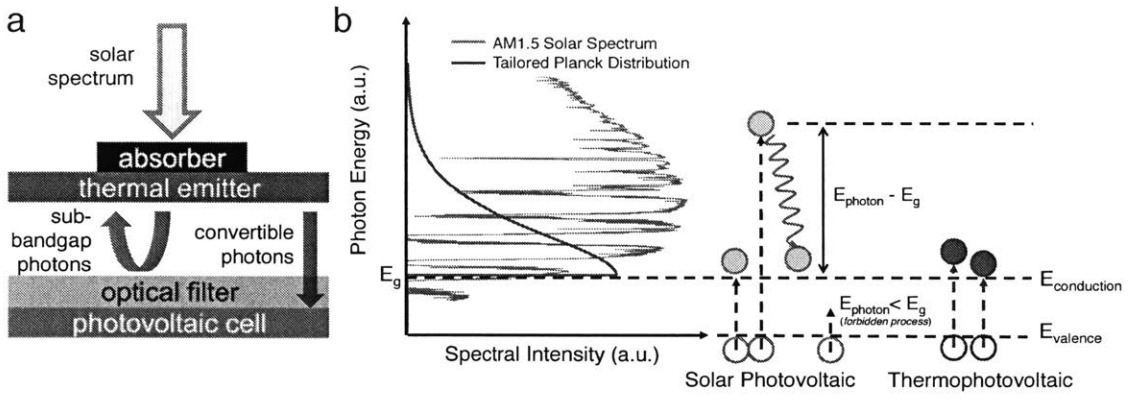

Figure 2: (a) Schematic representation of a solar thermophotovoltaic device. Incident concentrated sunlight is thermalized at the absorber. The generated heat conducts to the thermal emitter surface where, based on the temperature and spectral properties of the surface, engineered thermal emission is directed towards an optical filter. The filter passes photons capable of exciting charge carriers in a single junction PV cell and reflects to the emitter those which cannot. (b) Schematic of a thermally-based spectral conversion scheme. The STPV strategy generates an equivalent number of free electrons to the PV device but they are localized to the conduction band edge – drastically reducing heat generation in the diode.

2.2 THEORETICAL SPECTRAL ENHANCEMENT

In a STPV device, spectral engineering aims to restrict the thermal radiation reaching the cell to energies above a threshold ($E_{photon} > E_g$). The desired *effective* emissivity (achieved by suppressing[46] or reflecting[47] low energy emission modes) is a step function with unity emission relative to the blackbody at energies higher than E_g and no emission of sub-bandgap energy radiation (Figure 2b). At higher energies, the tail of Planck's distribution naturally limits the flux of photons with excessive energy ($E_{photon} >> E_g$). The theoretical limits of this type of single-cutoff energy STPV conversion deviate from the absolute upper bound previously published[23] based on monochromatic photon emission. Therefore, we first determined the limits of this strategy using a few assumptions: 1) the photo-thermal converter is perfectly black and is illuminated by fully concentrated sunlight, 2) the emission spectrum which illuminates the PV cell follows Planck's distribution at supra-bandgap energies and is null for sub-bandgap energies, 3) the PV cell converts the incident light (modified thermal radiation) using the assumptions described in the Shockley-Queisser limit[17] – allowing only radiative recombination from a black

PV converter, and 4) all non-essential losses are neglected. For more details about the model, refer to the Supplementary Information.

For a single-cutoff strategy, the temperature is a particularly important parameter since it determines the occupation of emission modes above the cutoff energy; as the thermal energy increases relative to the cutoff / bandgap, the supra-bandgap spectral distribution is enhanced and broadened. This is the basis for the fundamental tradeoff between power density and efficiency in STPVs. However, the choice of temperature for a particular bandgap is not trivial. The inset of Figure 3a shows three representative spectra which illuminate the same PV: 1) when the peak of Planck's distribution is aligned with E_g in *energy* space[48] ($k_b T_{emitter} = 0.35\, E_g$), 2) when the peak of Planck's distribution is aligned with E_g in *wavelength* space[49] ($k_b T_{emitter} = 0.2\, E_g$), and 3) when the Planck's distribution barely overlaps the energy bandgap ($k_b T_{emitter} = 0.1\, E_g$).

Figure 3a shows the maximum theoretical conversion efficiency as a function of the bandgap for different $k_b T_{emitter}/E_g$ ratios. A specific, optimum operating temperature for an ideal single-cutoff STPV exists, which depends on the bandgap of the material. If the thermal energy ($k_b T_{emitter}$) is high relative to E_g, an excess of high energy photons illuminate the PV; thermalization of these photons reduces the efficiency. At very high temperatures (i.e., large bandgaps), re-radiation losses from the absorber are also detrimental to the overall efficiency. On the other hand, smaller temperature differences between the hot (emitter) and cold (PV) reservoirs limit the extracted voltage level (in accordance with the Second Law of Thermodynamics) and thus the ultimate efficiency of the system.

Figure 3 shows how the spectral conversion approach described here can theoretically improve the performance of a solar-to-electrical conversion process over the entire range of the semiconductor materials used as long as the spectral converter temperature is selected appropriately. For the common Si PV cell (E_g = 1.1 eV), the maximum achievable efficiency for an ideal single-cutoff emitter STPV converter is 63%, ~40% greater than the Shockley-Queisser limit for this bandgap under fully concentrated sunlight. This efficiency is achieved at a rather high spectral converter temperature of 1600°C. For a low bandgap material, such as the one used experimentally in this work (InGaAsSb, E_g = 0.55 eV), the theoretical efficiency limit is ~60% greater than the Shockley-

Queisser limit, though the absolute performance is reduced. This efficiency, however, is attained at a more modest and practically achievable optimal temperature of 1200°C.

Figure 3b shows the undesired heat generated in each device, comparing solar PV to STPV, normalized by the amount of output electrical power produced. The STPV emitter temperature was optimized at each bandgap. For PV, the heat generation ratio is shown for a blackbody cell and for a cell with perfect reflectance below the bandgap (*i.e.*, an ideal back-surface reflector, BSR[50]). We included the latter case since the heat generated from sub-bandgap photons is not intrinsic to the solar PV process. For the low bandgap cell (E_g = 0.55 eV), the heat generated in the cell during the solar PV process is due to thermalization (down to E_g) of nearly the entire solar spectrum. The presence of a thermal spectral converter reduces the normalized heat generation in the cell by a factor of ~3. Reduced heat generation for the same or greater electrical power density relative to sunlight implies spectral enhancement.

However, real devices operate far from these limits because of losses such as: 1) non-radiative recombination and imperfect electrical transport in the cell and 2) parasitic heat losses via thermal radiation associated with the spectral converter, which take potentially convertible energy away from the PV cell. For a net benefit, the losses associated with spectral conversion must not exceed the additional useful flux delivered to the cell. The ratio of the two curves (PV to STPV) in Figure 3a indicates the lowest performance of a practical spectral converter compared to an ideal converter (no losses) that must be achieved in order for an STPV to outperform a solar PV (Figure 4). In the following section, we experimentally show the results of this spectral conversion process using engineered nanophotonic materials.

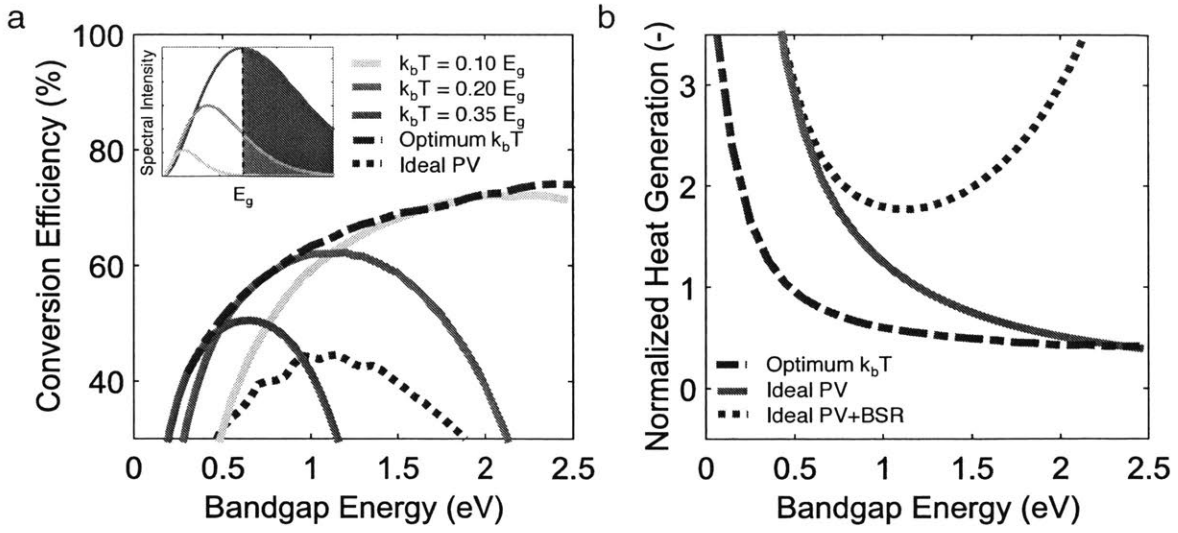

Figure 3: (a) Maximum theoretical conversion efficiency as a function of cell bandgap (E_g), comparing the Shockley-Queisser limit for solar PV to the single-cutoff STPV with an optimized converter temperature (T) and several specific k_bT/E_g ratios. Inset highlights the above-bandgap portion of Planck's distribution as function of increasing k_bT/E_g ratio. (b) Heat generation normalized to the output power density of each device. Short and long dashed curves for the ideal solar PV converter represent with and without spectral control, respectively.

The theoretical limits for the single cutoff energy scheme as described in this thesis were determined using a model that includes only essential losses. Both cases (*i.e.,* PV and STPV) follow the same model as described in Wu *et al.* and Lenert *et al.*[51], [52] asto treat the photovoltaic conversion as ideal. When illuminated by the solar spectrum, the model gives the same results as the Shockley-Queisser detailed balance formulation[17]. The ultimate power is calculated by assuming an EQE of unity above the PV's electronic bandgap, E_g

$$p_u = \int_0^{\lambda_g} \varepsilon_\lambda Q_{b,\lambda} \frac{\lambda}{\lambda_g} d\lambda \tag{1}$$

where $\lambda_g = hc/E_g$ (h is Planck's constant and c is the speed of light in vacuum) and $Q_{b,\lambda}$ is the spectral emissive power, determined by the blackbody temperature of the emitting body and its spectral emittance. This ultimate power, as in the previously mentioned publications, is reduced in two ways: X, the open circuit voltage (V_{oc}) is below the bandgap voltage (V_g) (equation (2)) and Y, the impedance must be matched to define the maximum output power that may be extracted from the single junction (equation (3)):

$$X = \frac{V_{oc}}{V_g} = \frac{k_b T_{PV}}{E_g} \ln\left(f \frac{R_{e,E>Eg}}{R_{PV,E>Eg}} \right) \tag{2}$$

where $R_{E>Eg}$ is the flux of emitted photons with energies above the bandgap.

$$Y = \frac{z_m^2}{(1 + z_m - e^{-z_m})(z_m + \ln(1 + z_m))} \tag{3}$$

Defined by the relation

$$z_m + \ln(1 + z_m) = \frac{eV_{oc}}{k_b T_{PV}} \tag{4}$$

Thus the final power density that may be extracted from the PV converter is given by

$$P_{\max} = p_u XY \tag{5}$$

The incoming power is simply the spectral integration of the incoming photon spectrum, $Q_{b,\lambda}$. The efficiency is the ratio of the maximum power, P_{max}, to the incoming power. For STPVs, this efficiency is multiplied by the essential photo-thermal efficiency which is derived in the blackbody limit. It is given by

$$\eta_{abs} = 1 - \left(\frac{T_{emmiter}}{T_{sun}} \right)^4 \tag{6}$$

The heat generation rate is calculated using a First Law analysis, requiring the difference in the input power and the sum of the electrical power density and essential losses to be generated as thermal energy.

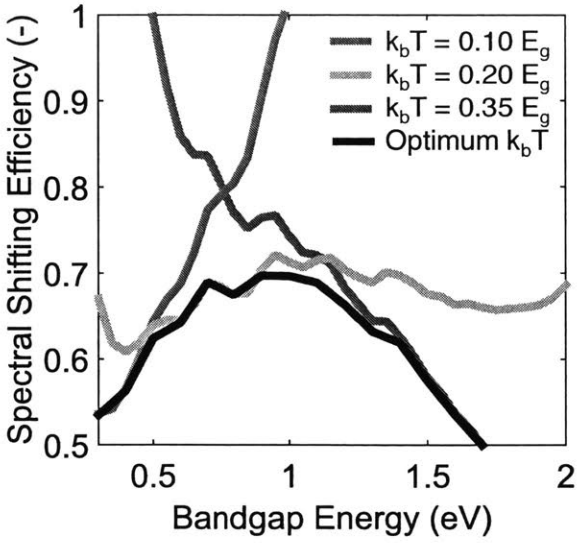

Figure 4: Ratio of the theoretical conversion efficiencies of solar PV to STPV represents the required performance of a realistic (with parasitic losses) spectral converter to match the solar PV efficiency.

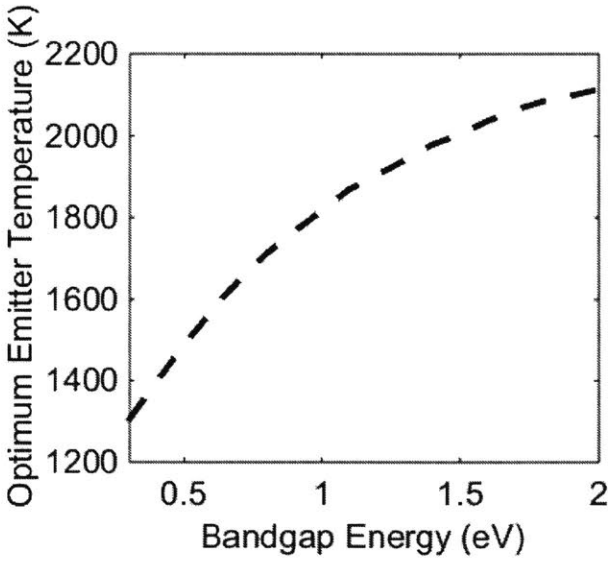

Figure 5: Optimum emitter temperature as a function of PV bandgap for a single cutoff emitter. Monotonic increase in temperature is expected in order to populate higher energy states.

2.3 NANOPHOTONIC MATERIAL SET

High photo-thermal efficiencies and precise spectral control are required to achieve properties similar to the ideal single-cutoff STPV system, such as the ones shown in Figure 3a. We used an InGaAsSb PV cell[38] (E_g = 0.55 eV) for our demonstration because the necessary operating temperature and spectral properties are not as stringent to achieve spectral enhancement at this bandgap. Incident sunlight is almost entirely absorbed within a multi-walled carbon nanotube (MWCNT) forest[27–29]. In principle, the introduction of spectral selectivity can further enhance the performance of a STPV, provided that reducing the emittance in the thermal wavelengths does not significantly reduce the absorption of incident sunlight. High solar absorptance is critical when the converter is subject to high optical concentration[51], as in our experiments. We fabricated a one-dimensional photonic crystal comprised of several Si/SiO_2 layers as the selective thermal emitter[36]. Both constructive and destructive wave interference provides a steep cut-off in the spectral emittance at the bandgap of the InGaAsSb PV cell[38]. However, >50% of the emitted power cannot be converted at the operating temperature due to the high intrinsic emission of the underlying Si at lower energies (<0.25 eV). Because this emission is a direct loss in the system[30], we incorporated a tandem plasma-interference rugate filter in this study through which the emitted light is passed. The filter was engineered to reflect low energy photons ($E_{photon} < E_g$) while transmitting the convertible ones ($E_{photon} > E_g$)[22,31].

Optical measurements of the participating surfaces in the spectral converter were used to simulate the resulting illumination spectrum on the cell at a few different emitter temperatures, shown in Figure 7b. Of the radiation arriving at the 0.55 eV cell, only ~20% of the energy is carried by photons below its bandgap at an emitter temperature of 1000°C and are therefore un-convertible. Qualitatively, we see the entire solar spectrum has been converted much closer to E_g (0.55 eV). Note, however, the conversion is not purely downward since 5% of the AM1.5D spectrum is below the bandgap of the cell. These photons are unable to generate electron-hole pairs if they were to directly illuminate the cell in a solar PV process. In this device, they are thermalized in the absorber and their energy may contribute to the emission of a convertible photon. This is a feature of STPVs that is distinct from other purely down-shifting strategies.

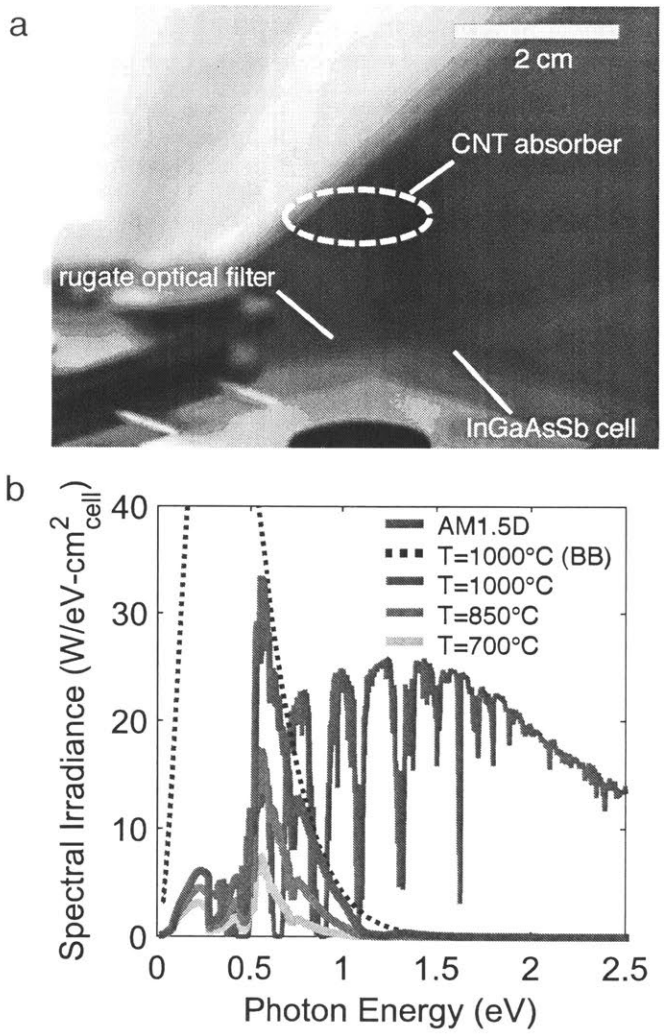

Figure 6: (**a**) Optical image of the solar thermophotovoltaic device constructed in this study to observe the spectral enhancement process. The backside of the suspended converter (not shown) is the Si/SiO_2 selective emitter. (**b**) The simulated spectral irradiances reaching the PV cell for a few different temperatures. Modification of the blackbody spectrum comes both from the spectrally selective Si/SiO_2 emitter as well as the rugate filter. Also shown is the AM1.5 solar spectrum at an optical concentration of 100 Suns (which is typical for STPVs with matching emitter and absorber areas[10].

2.4 EXPERIMENTAL SPECTRAL ENHANCEMENT

We performed a series of experiments to observe the enhancement of the converted spectrum using the material set previously described. We directly compared the operation of a cell with and without the presence of our spectral converter. To quantify the conversion performance of the device, we define efficiency as the ratio of electrical power generated by the device to the radiative power incident on the absorber surface

$$\eta_{device} = \frac{MPP_{PV}}{\dot{Q}_{solar}} = \frac{\dot{W}''_{elec} A_{PV}}{\dot{Q}_{solar}} \tag{7}$$

where MPP_{PV} is the maximum power operating point of the PV cell, $\dot{Q}_{solar}$ is the radiative power that impinges each absorber surface, $\dot{W}''_{elec}$ is the measured electrical power density, and A_{PV} is the total PV area in the device.

We first characterized the InGaAsSb[38] cell by exposing it to a simulated AM1.5D solar spectrum and varied the input flux over a wide range (50-100 suns). As expected, the generated photocurrent density scaled linearly with solar illumination in this range. The increasing photocurrent was accompanied by a logarithmic increase in open-circuit voltage and a slight decrease in fill-factor due to the presence of parasitic series resistance. This led to a relatively constant conversion efficiency which will be discussed later.

For comparison, we shielded the InGaAsSb PV from the solar spectrum with the spectral converter and repeated the experiment. We designed our spectral converter to be 4 cm^2 in order to drastically improve the thermal performance from our previous work (1 cm^2)[17]. This scale up decreased the amount of side losses relative to the primary radiation flows. Due to the limited availability of the InGaAsSb cells, we used the same converter (1 cm^2) as the first experiment. Thus, inactive PV cells were arranged below the filter which participated radiatively, but not electrically, to match the emitter area (3 cm^2 of inactive cells + 1 cm^2 of active cells, Figure S3a). Due to the high reflectivity of the rugate filter at sub-bandgap energies (Figure 7), the effect of the inactive PV cell area on the energy balance was negligible.

Given the geometry of the spectral converter, thermal gradients due to the spreading of absorbed power in the CNT forest, and local view factor variations are expected. To address this, we took advantage of the symmetry of the device – the net radiation exchange in any one of the four quadrants on the emitter surface are spatially equivalent. Thus the average photocurrent density generated in the active PV cell is representative of the entire emitter area. For the STPV testing, the MPP_{PV} was determined by finding the $MPP_{active\ PV}$ and scaling it to meet the total PV area, validated by the experiments shown in the following figure.

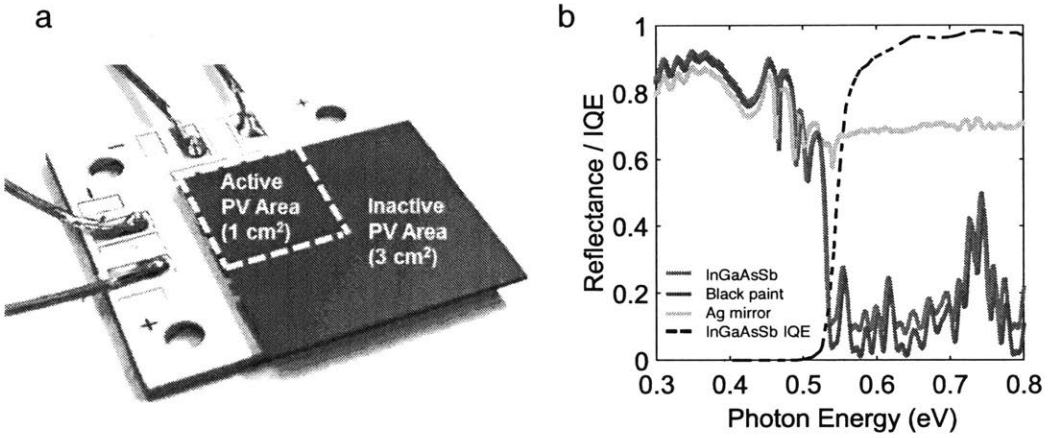

Figure 7: (**a**) The 4 cm^2 PV, with a bonded optical filter covering the 4 cells. The active PV participates radiatively and electrically while the inactive PV participates only radiatively. (**b**) FTIR reflectance spectra of the rugate filter bonded to different substrates. The optical properties of the rugate / black paint combination are much closer to those of the rugate / Ag combination. Also shown is the spectral response of the underlying InGaAsSb PV converter.

As in the solar PV test, we varied the incident radiation on the absorber and recorded the electrical characteristics of our active PV cell. Two different STPV devices were tested. One of them (STPV 1) had a smaller absorber relative to the emitter surface area $\left(\frac{A_{emitter}}{A_{absorber}} = 12\right)$ and the other (STPV 2) had a larger absorber $\left(\frac{A_{emitter}}{A_{absorber}} = 7\right)$. The smaller absorber demonstrated reduced thermal re-emission losses and therefore more efficient device operation. The input power to all devices (solar PV and STPV) was provided by our solar simulator (*92192, Newport Oriel, Inc.*); in some STPV cases, this light source was supplemented by a Xenon-arc broadband source (*66475, Newport*

Oriel, Inc.) to achieve higher emitter temperatures. More about the optical configuration is provided in the Supplementary Information.

2.5 EFFICIENCY COMPARISON

Figure 8a shows that while the conversion efficiency of the solar PV process remained relatively constant with increasing output electrical power, the measured STPV efficiency reached 6.8 +/- 0.2%, which is ~2x higher than previously reported values of comparable measurements. Our experimental results (shown as points) show good agreement with our isothermal radiative transfer model (shown as smooth lines, see our previous work[32] for a more details). At low output power densities, the device conversion efficiency of the PV cell was much higher than that of the STPV device since the thermal emitter remained at insufficiently low temperatures (the overlap of Planck's distribution with the bandgap of the PV cell determines generated photocurrent). However, as the emitted photon flux became more energetic at higher temperatures (Figure 6b), there was a transition to a regime where the spectral conversion strategy exceeded the overall efficiency of the solar-to-electrical conversion of the directly illuminated cell (solar PV).

This experimental demonstration of an STPV device exceeding the performance of solar PV with the same cell successfully exhibits the enhancement gained from spectral conversion; the losses introduced by the absorption / re-emission process were outweighed by the improvement gains from converting the solar spectrum. Our model (described in Ref. 19) indicates that at our highest measured efficiency point, ~68% of incident power was delivered to the cell in the form of a modified spectrum, ~10.2% of which was converted by the cell into electrical power. Our model suggests that increasing the input power further (and therefore $T_{emitter}$) would allow the STPV device to continue to exceed the conversion efficiency of this PV cell and reach overall efficiencies approaching 10% for this particular experiment.

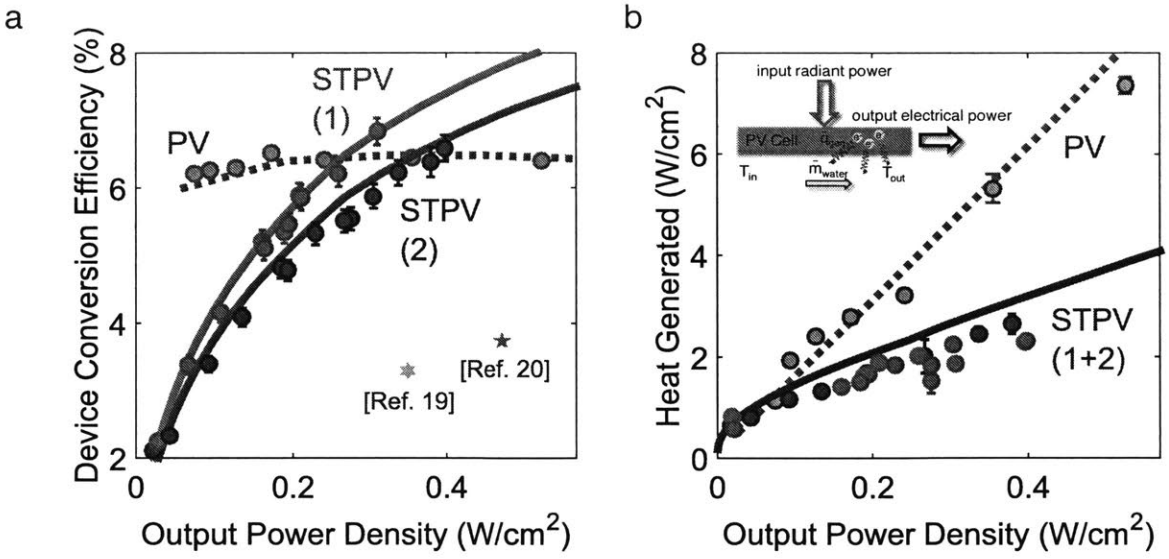

Figure 8: (**a**) Converter device performances for both STPV and PV with InGaAsSb (E_g = 0.55 eV) cell. The STPV exceeds the PV conversion efficiency for a given output power density at sufficiently high temperatures. Increasing the input solar power is expected to raise the emitter temperature and increase further the conversion efficiency relative to the PV cell. STPV (1) has a smaller absorber than STPV (2) and thus operates more efficiently for a particular output power. (**b**) Heat dissipated by the cooling loop in both the PV and STPV experiments in order to maintain the PV converter at an equilibrium temperature (Supplementary Figure 4). Reducing the illumination of the PV cell with unusable photons improves efficiency and dramatically reduces heat generation.

2.6 HEAT GENERATION AND THERMAL MANAGEMENT

From a heat generation perspective, the two spectra (solar and modified) shown in Figure 3b produced dramatically different heat loads on the cell. Since the bandgap of the InGaAsSb cell is energetically almost entirely below the solar spectrum, a large portion of the incident energy contributed to heat generation. When the cell is illuminated by the lower energy spectrum that is produced by the spectral converter, the resulting heat generation is substantially reduced. Figure 8b shows the measured heat generation in the PV cell for the experiments. At 0.35 W/cm^2 of electrical power density, the solar PV generated ~2x more thermal power in the cell than the STPV despite having the same conversion efficiency (to within the error of the measurement). Excessive

heat loads must be dissipated with higher convection coefficients to prevent an increase in cell temperature and thus reduced electrical performance[33].

Heat generation was further quantified by monitoring the cell temperature in each experiment as well as the degradation in cell performance as a function of temperature. This data is shown in the following figure.

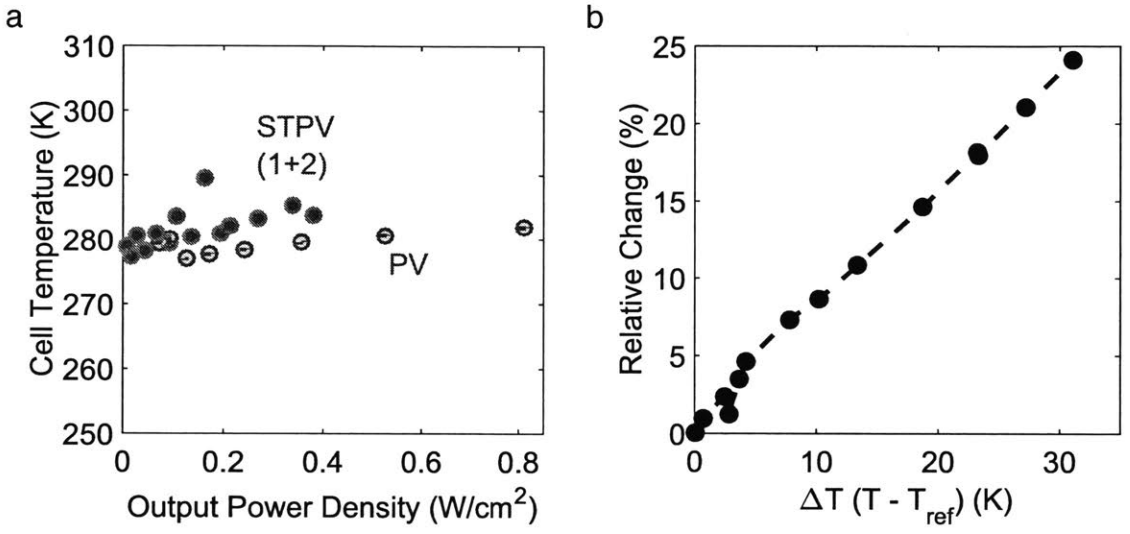

Figure 9: (**a**) Temperature obtained by a type J thermocouple sandwiched between the PV cell and the copper cooling block during the recording of each data point. Cell temperatures do not vary more than 6 K between the large absorber STPV and PV runs, with the STPV cell being slightly warmer. (**b**) Relative change in power produced by the PV cell for a given constant input spectrum while varying the temperature.

2.7 DISCUSSION

This experimental demonstration of spectral enhancement using a single-cutoff scheme provides deeper insight into the conversion process. The transformation of the solar spectrum into a narrow band thermal spectrum is, in principle, independent of the quality of the PV cell used in the device. By revisiting the idealized PV cell introduced in the theoretical section which operates at the Shockley-Queisser limit under a given solar illumination, we show in Figure 10 that incorporating

our spectral converter would enhance the conversion rate and thus exceed this limit, despite an un-optimized design and non-ideal spectral components (provided the input beam could be further concentrated for sufficient thermal performance). According to the analysis, the crossover points at which the STPV meets the Shockley-Queisser limit occurs at an emitter temperature of ~1300°C and an optical concentration of ~2000x on the absorber (~200x on the idealized PV due to the introduced area ratio). However, a spectral converter constructed of the same material set, but at the ~kW scale where parasitic heat losses from the supports and device edges are negligible, would further improve the efficiency of this converter by ~10-15%. The crossover point in this case is at a moderate emitter temperature of ~1000°C and an optical concentration of ~800x (~80x on the idealized PV). Thus, moving to larger devices plays an importance role in exceeding the Shockley-Queisser limit at more feasible operating conditions. Included in the figure are the results from the ideal single-cutoff emitter used to calculate the theoretical limits, indicating that our demonstrated spectral converter is only ~15% worse than this ideal case.

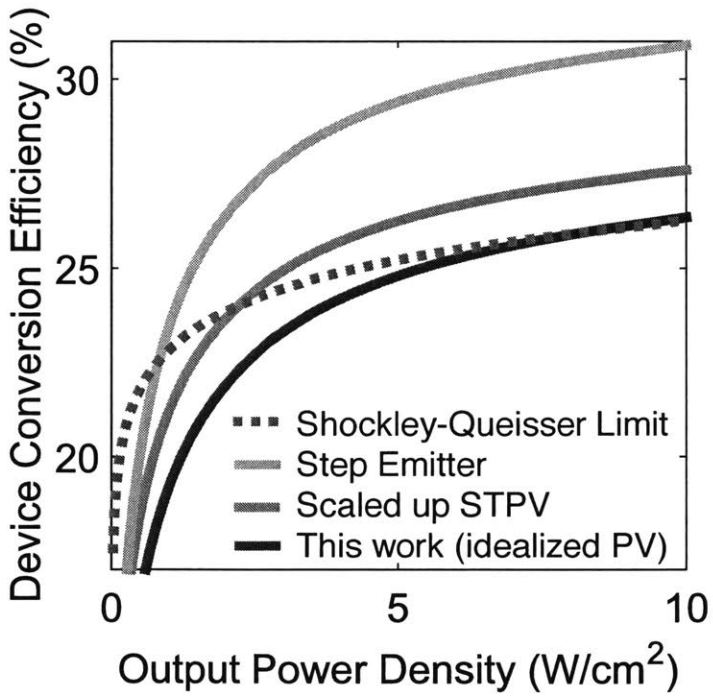

Figure 10: Conversion efficiencies of the devices in the radiative limit. By replacing only the PV cell, our demonstrated material set could exceed the Shockley-Queisser limit at sufficiently high temperatures. Also shown is a prediction of our scaled up device that has negligible parasitic heat loss.

2.8 CONCLUSIONS

Any spectral modification strategy implemented between the sun and a PV needs to perform well enough to justify the losses introduced to the system. While this demonstration was performed on a low bandgap cell, our theoretical analysis shows this thermally-based spectral enhancement can be extended to wider bandgap materials to reach higher efficiencies. As the development of refractory photonic materials continues to grow rapidly, higher quality emission spectra will be delivered to the PV cell. Future studies should continue to seek high spectral control with cost-effective and scalable components as the field begins to approach commercializable solar energy converters.

2.9 METHODS

The absorbing and emitting surfaces were prepared using standard physical and chemical vapour deposition (PVD, CVD) processes. The Si/SiO_2 layers of the one-dimensional photonic crystal were deposited by low-pressure (LP) and plasma-enhanced (PE) CVD[36]. The rugate filter was purchased by *Rugate Technologies, Inc.* Optically transparent[34] polydimethylsiloxane (PDMS) was used to epoxy the cold-side rugate filter directly to the InGaAsSb PV cell.

The MPP_{PV} was determined by *in situ* quasi-steady current-voltage sweeps during operation (*Keithley 2440*). $\dot{Q}_{solar}$ was measured at the absorber plane using a thermopile detector (*919P-040-50, Newport*) for each MPP_{PV} data point recorded. To quantify the heat generation in the PV cell during the conversion process, we monitored the amount of heat dissipation required to keep our converter at a fixed temperature (Supplementary Figure 4). This was performed using a cooling loop in thermal contact with the PV cell via a thin copper block. The inlet and outlet temperatures of the water that passed through the copper block were measured with two thermocouples (*Type J, Omega Engineering*) and we regulated the flow rate with a peristaltic pump (*Masterflex EW-07522-20, Cole-Parmer*). Both the PV and the STPV heat generation data were acquired without an external electrical load and were corrected accordingly. The spectral converter

and PV cell were aligned and placed in an evacuated environment (<0.5 Pa). The emitter was held approximately 300 μm apart from the surface of the rugate filter (thickness of 400 μm) using a giving a diffuse view factor with the PV cell of 96%.

Uncertainty in the reported experimental values was evaluated based on propagation of the following errors: standard deviation (using a *t*-distribution with 95% C.I.), instrument error, and resolution error.

Chapter 3

3. Bridging the Efficiency Gap

3.1 INTRODUCTION

In recent years, the demonstrated efficiency of solar powered thermophotovoltaic devices (STPVs) has improved greatly[7], [10], [44], [59]. This improvement has come primarily from a focus on high spectral control through the design of micro-/nano-scale structures used to tailor the high-temperature thermal emission spectrum with the goal of both efficiently capturing sunlight and suppressing the illumination of the photovoltaic cell (PV) with sub-bandgap radiation. In addition, steps have been taken to integrate these nano-engineered surfaces into larger devices to understand and control the flow of thermal energy to improve the overall performance.

In this thesis, we have reported the highest solar-to-electrical conversion efficiency of a STPV at the time of this publication of 6.8%[59]. When compared to the fundamentally limiting Carnot efficiency between the hot and cold temperatures in the device (~85%), there is a large discrepancy. Where does all the power go? The answer to this question has large implications for the research field and motivates questions about the theoretical limits for STPVs generally.

This chapter discusses the highest achievable STPV efficiency by considering the limiting phenomena associated with both solar thermal and photovoltaic energy conversion. We present a theoretical limit which is lower than what has previously been published[6] by taking into account intrinsic recombination mechanisms in the PV cell. We then build upon this model to include realistic characteristics of the PV, emitter, and solar absorber to understand which aspects must be developed to begin to approach the fundamental limitations of STPV conversion.

3.2 THEORETICAL LIMITS OF STPV

The theoretical limit for STPVs has been presented in [6] and it is generally understood that the device could not surpass the Blackbody Limit[60] given by:

$$\eta_{max}(T_h) = \left(1 - \left(\frac{T_h}{T_s}\right)^4\right)\left(1 - \frac{T_c}{T_h}\right) \tag{1}$$

which suggests that the limiting efficiency is a product of the efficiency of the best solar thermal absorber and a Carnot engine. Essentially this is a solar-driven Carnot cycle. The first term, which includes the quotient of the fourth power of the absorber and Sun blackbody temperatures, represents a perfect radiative exchange between a blackbody absorber and the Sun. It decreases monotonically with increasing T_h. The second term represents the efficiency of the ideal heat engine which is taken in the limit of open-circuit voltage for the PV. It can be shown that this limit will recover a Carnot efficiency. The function can be maximized by finding the zeros of the derivative of the efficiency with respect to T_h:

$$\frac{d(\eta_{max})}{dT_h} = \frac{-4T_h^5 + 3T_h^4T_c + T_s^4T_c}{(T_h^2T_s^4)} = 0 \tag{2}$$

$$T_{h,max} = 2444\ K, \eta_{max} = 84.7\% \tag{3}$$

However, this only represents the limiting efficiency between an emitter at T_h and a "cold-side" at T_c which is incapable of producing finite power. Instead, we will now consider the case where the emitter at T_h will be in contact only with an ideal PV cell at T_c which is held at some operating voltage, V, through which power is extracted.

To begin the analysis, we first consider a thought experiment for an ideal TPV system. The thermal emitter communicates with the PV cell only through a perfect optical filter. Namely, this filter will pass photon wavelengths corresponding to the bandgap energy of the PV cell, E_g. The photons that transmit are perfectly absorbed within the PV and contribute to the generation of an equal amount of electron-hole pairs. Those carriers are extracted by an applied voltage across the cell.

During the process, the cell will also emit some amount of photons with energy E_g which can therefore escape back through the filter to the emitter surface (where they will be absorbed with 100% probability).

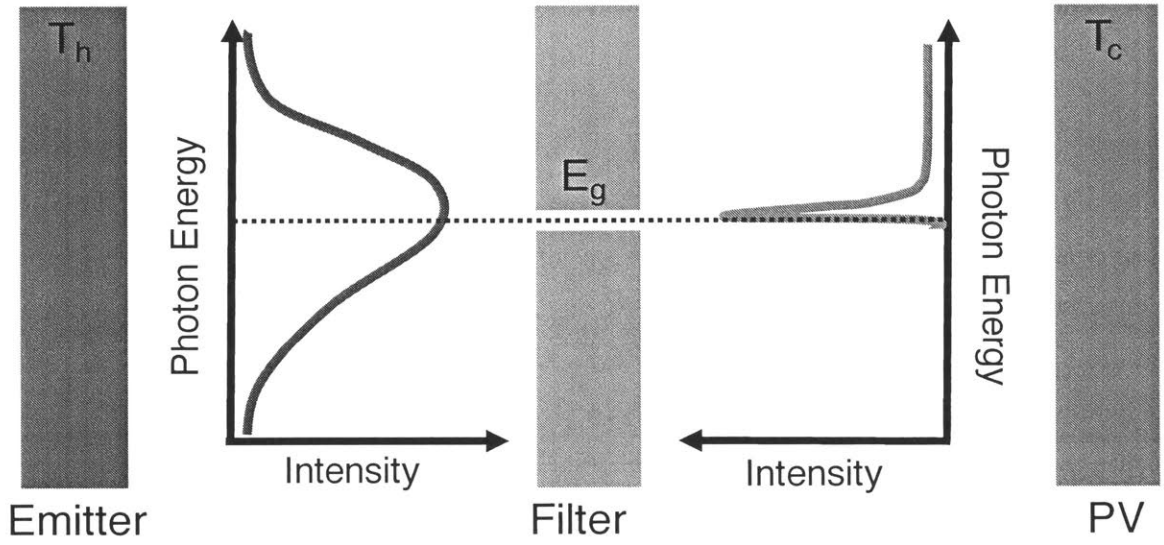

Figure 11: Schematic representation of the limiting TPV efficiency case. A broad emission spectrum illuminates an ideal optical filter that only passes photons with energy levels matching the bandgap of the PV cell. When power is extracted from the PV cell, some photon spectrum is created that sends power back to the hot emitter.

We balance the current fluxes in the radiative limit by calculating the different between the generated carriers and the recombined carriers:

$$I(V) = q(photon\ flux\ in - photon\ flux\ out)$$

$$= q\left(\frac{2\pi f^3}{c^2}\frac{1}{\exp\left(\frac{E_g}{kT_h}\right)-1} - \frac{2\pi f^3}{c^2}\frac{1}{\exp\left(\frac{E_g - qV}{kT_c}\right)-1}\right) \quad (4)$$

Equation 4 can be simplified to:

$$I(V) = \frac{2\pi f^3 q}{c^2}\left(\frac{1}{\exp\left(\frac{E_g}{kT_h}\right)-1} - \frac{1}{\exp\left(\frac{E_g - qV}{kT_c}\right)-1}\right) \tag{5}$$

The power density that can be extracted from this diode is the product of this current density and the applied voltage:

$$P_{elec} = \frac{2\pi f^3 qV}{c^2}\left(\frac{1}{\exp\left(\frac{E_g}{kT_h}\right)-1} - \frac{1}{\exp\left(\frac{E_g - qV}{kT_c}\right)-1}\right) \tag{6}$$

Where f is the photon frequency, q is the elementary charge, c is the speed of light, and k is the Boltzmann constant. The net radiative power leaving the emitter is given by:

$$P_{emit} = \frac{2\pi f^3 E_g}{c^2}\left(\frac{1}{\exp\left(\frac{E_g}{kT_h}\right)-1} - \frac{1}{\exp\left(\frac{E_g - qV}{kT_c}\right)-1}\right) \tag{7}$$

The ratio of equations 6 and 7 define the efficiency of this monochromatically illuminated TPV (MIT-PV) device:

$$\eta_{MIT-PV} = \frac{qV}{E_g} \tag{8}$$

where V can be any value ranging between 0 and $(1\text{-}T_c/T_h)E_g$. The upper bound is determined by setting the total number of charge carriers equal to 0 and solving for V. For finite powers, however, equation 6 should be maximized which will recover the voltage corresponding to maximum power as well as the total output power density. Equation 6 is an implicit function, and can be solved using any number of different optimization techniques.

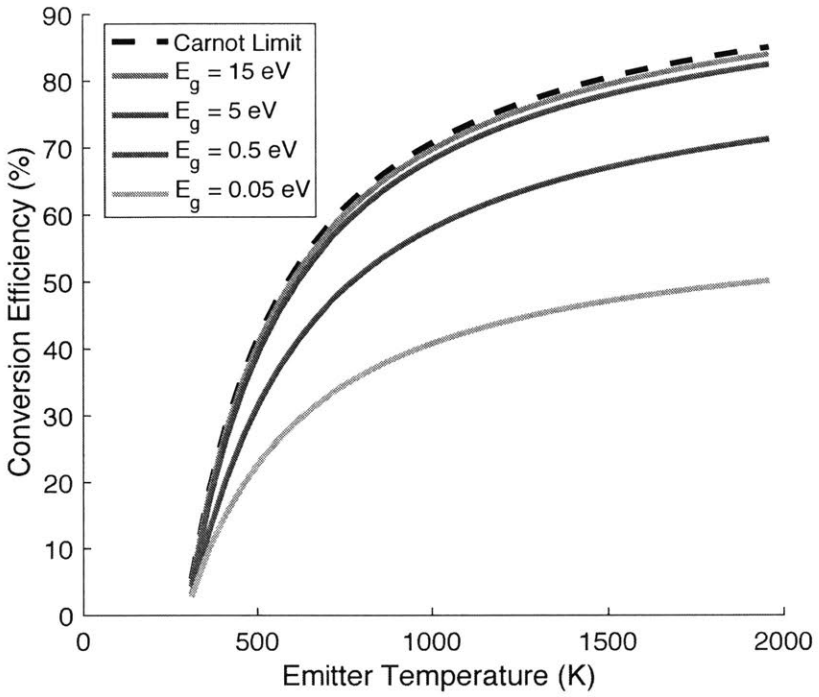

Figure 12: Maximum conversion efficiency considering finite power extractions for a MIT-PV device.

Figure 12 shows the conversion efficiency for a few different cases as a function of T_h with T_c staying at a fixed value of 300 K. All cases are bounded from above by the Carnot efficiency between the two temperatures. As the bandgap gets higher for a given temperature, the efficiency as given by equation 8 begins to asymptotically approach the Carnot efficiency. For extremely high bandgaps, the thermal emission spectrum contains only small photon populations. This limit essentially means that the photocurrent goes to 0 and the diode operates at open circuit conditions. Equation 8 indicates that the resulting efficiency will in fact be equal to Carnot.

At lower bandgaps, such as those of Ge, GaSb, InGaAs, InGaAsSb, etc., the generation of power will necessarily force the efficiency below the limiting Carnot efficiency. This effect is shown in Figure 13, below. For InGaAsSb, with E_g = 0.55 eV, the maximum conversion efficiency when monochromatically illuminated with a T_h = 1500 K source is 67%.

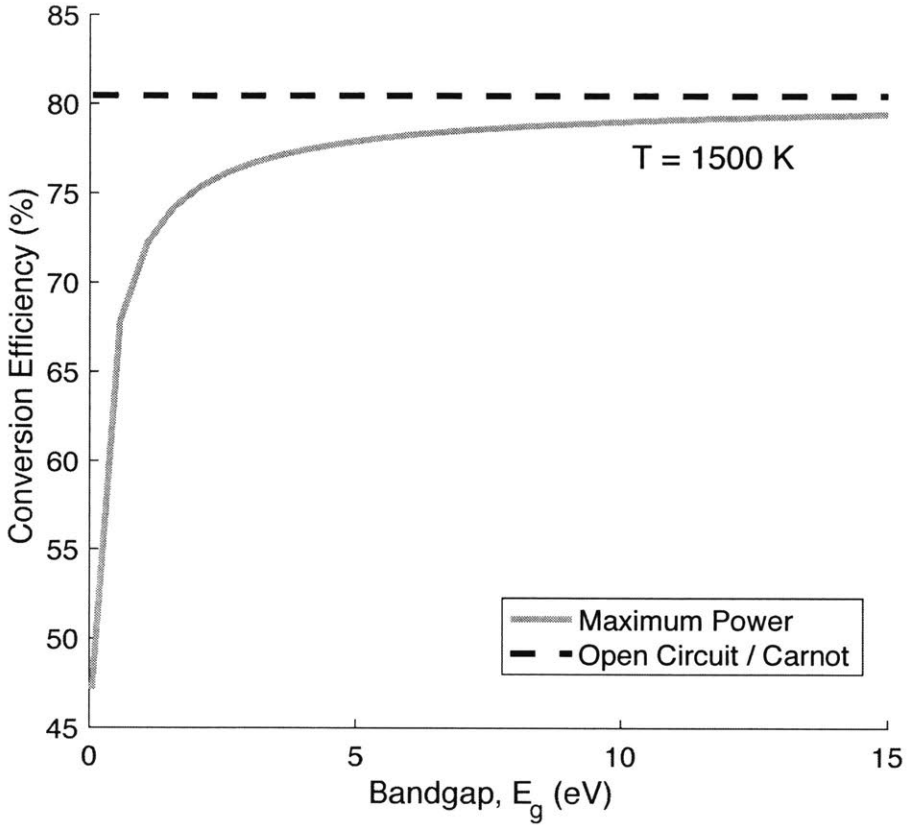

Figure 13: The theoretical conversion efficiency as a function of bandgap comparing the case of maximizing power out of the device to the open-circuit conditions. In the radiative limit, open-circuit conditions yield the Carnot efficiency.

The next logical modification of this model is to broaden the illumination spectrum so that it changes from a "delta" function to a "pulse" function. In other words, instead of only passing photons with energies equal to the bandgap, E_g, this lossless optical filter passes all photons with energies greater than or equal to E_g. In this case, it is important to optimize the temperature of the emitter relative to the bandgap energy as discussed in the previous chapter. However, if just a single temperature is considered (T_h = 1500 K), then the effects of increasing the spectral width are shown in Figure 14, below.

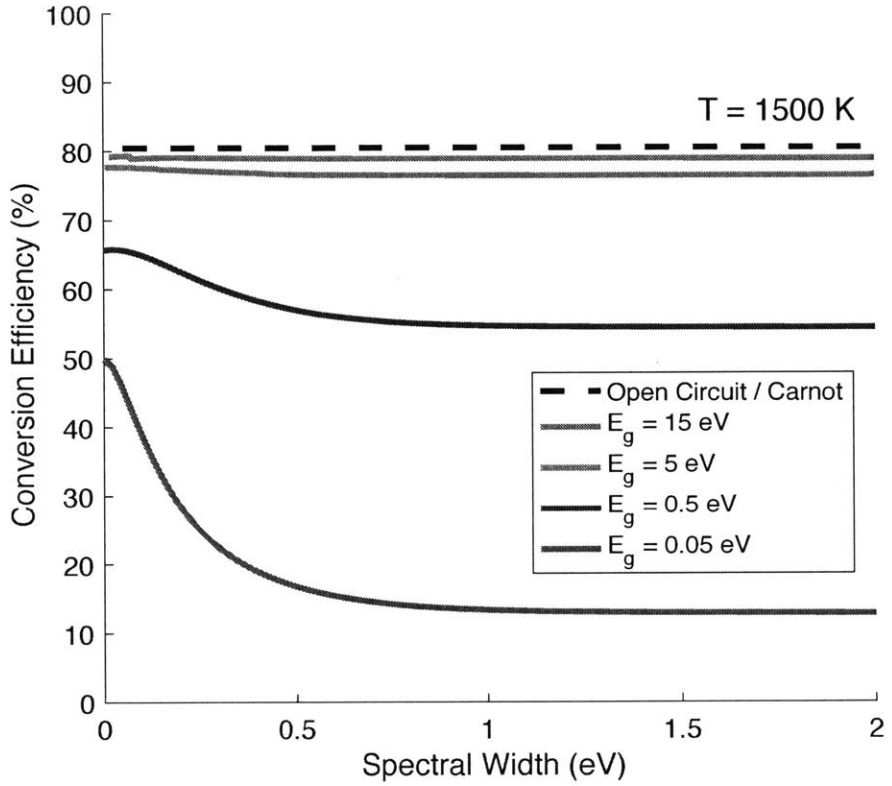

Figure 14: The effect of broadening the above-bandgap spectral width on the TPV conversion efficiency. The efficiency of the high bandgaps is insensitive to this width as there are small photon populations at those high energies for this temperature. The effect is larger for lower bandgaps as the majority of the photon spectrum lies at higher energies than their bandgaps.

For a 0.55 eV bandgap, the effect of broadening the spectral width on the overall efficiency is not large. The conversion efficiency goes from ~65% to ~55% as the broadening varies from monochromatic to blackbody (disregarding sub-bandgap photons).

Up to now, we can understand that the main losses in efficiency from Carnot have to do with 1) the radiative recombination from the ideal p-n junction and 2) the broadening of the spectral width as one deviates from monochromatic illumination. These losses bring the fundamental limit from ~85% to ~55% based on the operating principle of "step-function" TPVs. In the next section we will discuss the reduction in power associated with other, non-radiative, recombination mechanisms within the PV cell.

3.3 DEPARTING FROM THE RADIATIVE LIMIT

Another major reduction in efficiency from the ideal case to our experimental results is due to relatively low open-circuit voltages from the diode relative to the bandgap. This is a direct result of the different recombination mechanisms in the cell. We have already discussed the effect of radiative recombination and how that contributes to reducing the cell voltage from the bandgap energy. These other mechanisms are accounted for by reformulating equation 5 to a form that allows us to compare recombination rates[61]:

$$I(V) = q\left(\int_0^{\lambda_g}\left(\frac{\lambda}{hc}\right)Q(\lambda,T)\,EQE(\lambda)d\lambda - e^{\frac{qV}{kT}}\int_0^{\lambda_g}\left(\frac{2\pi c}{\lambda^4}\right)e^{-\frac{hc}{kT}}d\lambda - R_{SRH}\,e^{\frac{qV}{2kT}} - R_{aug}e^{\frac{3qV}{2kT}}\right) \tag{9}$$

$$I(V) = q\left(G_{ph} - R_{rad}e^{\frac{qV}{kT}} - R_{SRH}e^{\frac{qV}{2kT}} - R_{aug}e^{\frac{3qV}{2kT}}\right) \tag{10}$$

Where R_{SRH} is the rate of recombination for Shockley-Read-Hall Recombination[62], R_{aug} is the rate of recombination for Auger Recombination[62], and G_{ph} is the rate of carrier generation in the p-n junction. This form allows us to isolate the contributions of these different recombination mechanisms on reducing the open-circuit voltage as well as the maximum power point. These recombination rates are reported for several different TPV semiconductors. For the case of this study, we will use literature values for InGaAsSb[61], [63], [64] since we are trying to understand our experimentally reported efficiency value of 6.8%. However, we can go through this exercise for any semiconductor.

We can further understand this through the recombination lifetime parameter. The recombination lifetime is the reciprocal sum of each recombination mechanism:

$$\frac{1}{\tau} = \frac{1}{\tau_{rad}} + \frac{1}{\tau_{SRH}} + \frac{1}{\tau_{Aug}} \tag{11}$$

Thus the overall recombination lifetime will be governed by the shortest lifetime. The effect of Auger recombination will compete with the radiative recombination to determine the limiting voltage that can be generated by the p-n junction since it is a fundamental process which cannot

be reduced for a given material set. We have calculated the radiative recombination lifetime of ~10 ns and the Auger recombination on the order of ~1 ns which is consistent with [65].

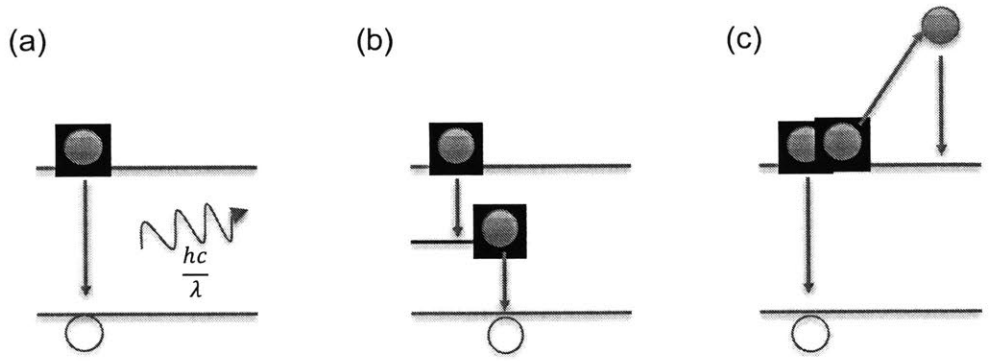

Figure 15: Schematic representation of the three different dominant radiative and non-radiative recombination mechanisms. (a) Radiative recombination wherein a band-to-band transition results in the emission of a photon with energy dictated by the electronic bandgap. (b) Non-radiative recombination through a defect or an intermediate energy state known commonly as Shockley-Read-Hall recombination. (c) Non-radiative recombination wherein a free electron imparts its energy on another free electron, raising its energy state to deep into the conduction band where phonon interactions quickly thermalize the electron back to the band edge. The electron that gave away its energy recombines with a hole. This is known as Auger recombination.

A common way that these parameters are lumped together is through the reporting of a saturation current density, I_0. This parameter is defined as the leakage current in the absence of light. The higher the saturation current, the lower the open circuit voltage will be. The diode equation for a solar cell without considering ohmic losses in the circuit is then given by:

$$I(V) = qG_{ph} - I_0 e^{\frac{qV}{nkT_c}} \tag{12}$$

Equation 12 is identical to equation 10, where the recombination rates are captured through the saturation current pre-exponential term. Equation 12 also assumes that $qV / kT_c >> 1$ which is often true during TPV operation[66]. To understand the reduction in voltage from a case of purely radiative recombination, the maximum efficiency as a function of the dark current density, I_0.
we include saturation currents from literature for both the quaternary InGaAsSb cell that was used in our experiments[38] of ~10^{-5} A/cm^2 as well as for slightly higher bandgap cells, such as InGaAs, with a reported saturation current of ~10^{-8} A/cm^2. At $T_{emitter}$ = 1500 K, this corresponds to a loss of voltage of 110 mV and 80 mV, respectively. Given the low bandgaps, this represents a substantial loss of power.

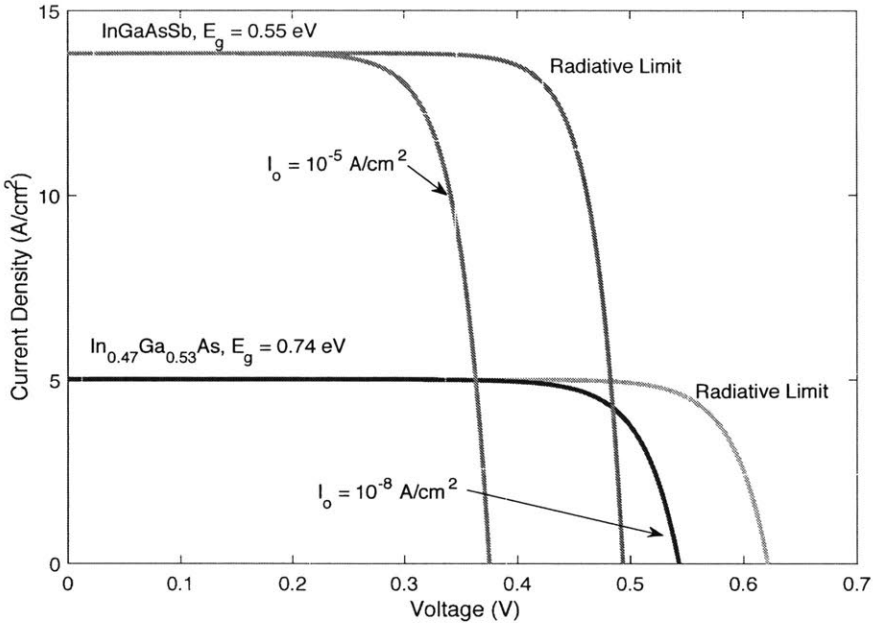

Figure 16: Current – voltage characteristics for two different diodes shown under ideal step-function illumination. The drop in open-circuit voltage is a direct result of the dominant, Auger recombination which sets a more practical limit than the radiative limit. For both diodes, literature values of the Auger recombination coefficient and carrier concentrations are used.

If we continue from the assumption that our emitter gives full illumination above the PV's bandgap and can suppress all sub-bandgap emission (still a hypothetical framework), then we can see the contribution of these non-radiative recombination mechanisms on the deterioration of the open-circuit voltage and therefore the maximum power extracted from the diode. Assuming the cell is at T_c=300K, we assume the following parameters[67]–[69]:

Table 1: Assumed electronic properties from literature values.

Parameter	Value
Carrier Diffusivity	40 cm^2/s
Intrinsic carrier concentration	$1.3x10^{13}$ cm^{-3}
Electron / hole concentration	$1x10^{18}$ cm^{-3}
Emitter thickness	3 μm

Using these values, we can investigate the effect of recombination lifetime (as dictated by Auger recombination in the limiting case) in determining the diode's saturation current as well as the overall efficiency for step-function TPV operation.

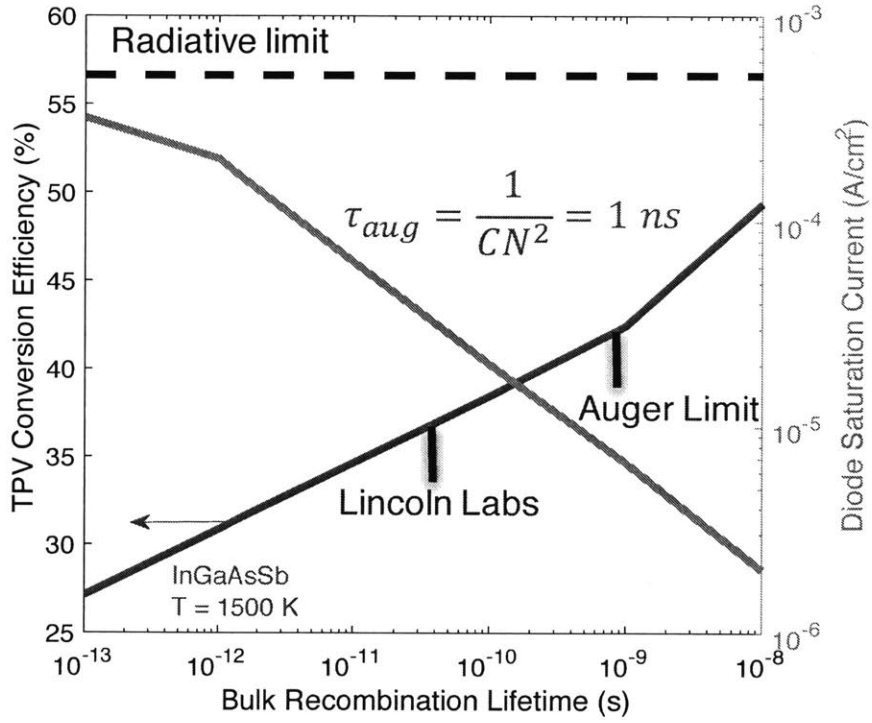

Figure 17: The effect of bulk recombination lifetime on the diode saturation current and the TPV conversion efficiency. A lifetime of ~1 ns corresponds to the Auger limited cell where the saturation current is about 10^{-5} A/cm^2. This corresponds to a maximum efficiency of ~43%. The

cells fabricated by Lincoln Labs[38] used in our experimental work have a dark current closer to $3x10^{-5}$.

We calculate that for this InGaAsSb cell, limited ultimately by Auger recombination, the maximum efficiency we can sustain is 43.4% and the actual fabricated cell[38] can only achieve an efficiency of 36.6%.

3.4 THE EFFECT OF NON-IDEAL ILLUMINATION

A major assumption up to this point in our analysis has been the ideal monochromatic illumination or the semi-ideal step-function illumination. In this section, we introduce the measured spectral properties of our TPV device including the quantum efficiency, the emitter emittance, and the optical filter transmittance. These properties were reported in the experimental chapter of this thesis. Taking these non-idealities into account, we can see the different spectra in Figure 18.

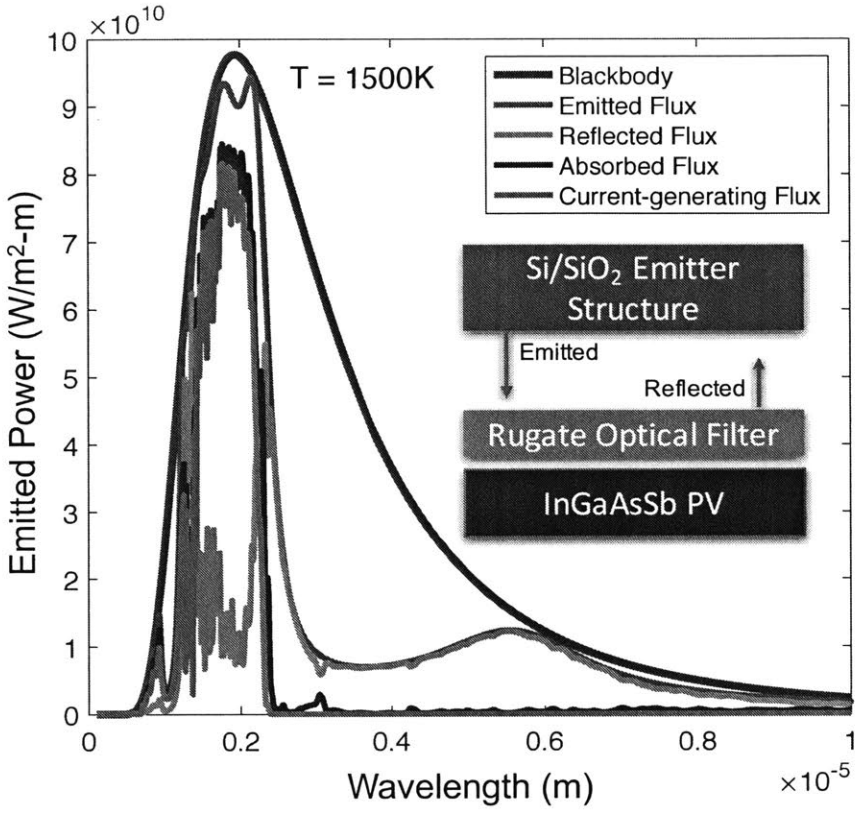

Figure 18: Spectral properties of our system showing for each relevant wavelength what portion of the blackbody is: emitted, reflected, absorbed by the PV, generates excitonic energy.

Presented in this way, it is difficult to determine how these spectral properties contribute to decreasing the maximum efficiency of our system. By looking at a cumulative function of emitted power as a function of wavelength, however, we see the critical importance of spectral matching.

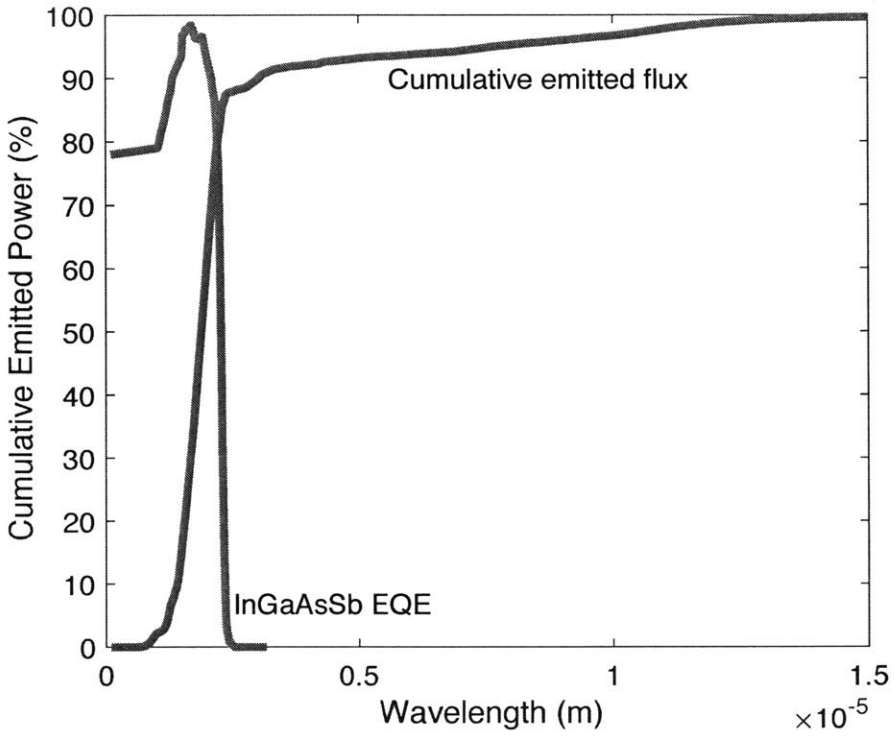

Figure 19: The cumulative emitted flux as a function of photon wavelength in the system. Also shown is the spectral response of the InGaAsSb cell for reference.

Figure 19 shows that for low wavelengths, the cumulative emitted power increases as we expect, determined by the high-energy tail of the Planck distribution. When the slope begins to rapidly decrease, it indicates the transition between high emission / transmission and low emission / transmission from the selective emitter – filter material set. From the plot, we can see that when the cumulative emitted power is close to 80% (~2.2 μm), the quantum efficiency is at 60%. Moreover, when the cumulative emitted power is at 60%, the quantum efficiency falls below 90%. So, 20% of this power will undergo roughly a 25% loss due to incomplete absorption near the band edge. The remaining 20% of power that is emitted below the bandgap will be completely lost. To reiterate, this shows the importance of spectral matching when designing a photonic crystal structure. It is better to have low emission where there is high EQE than to have high emission where there is low EQE. Considering non-ideal illumination, the limiting efficiency of our TPV engine is 26.6%.

3.5 EXPERIMENT-SPECIFIC LOSSES

The solar-driven TPV device that was presented in this thesis was still ~4x lower performing than this limit. The reason is due to a collection of losses that are not exactly fundamental to the material set we explored. The series and shunt resistances of the circuit were extracted from the current-voltage relationship and they were used to determine further loss in power. The resistance values were 0.03Ω and 300 Ω, respectively. The effect of the non-ideal electrical transport can be seen in Figure 20.

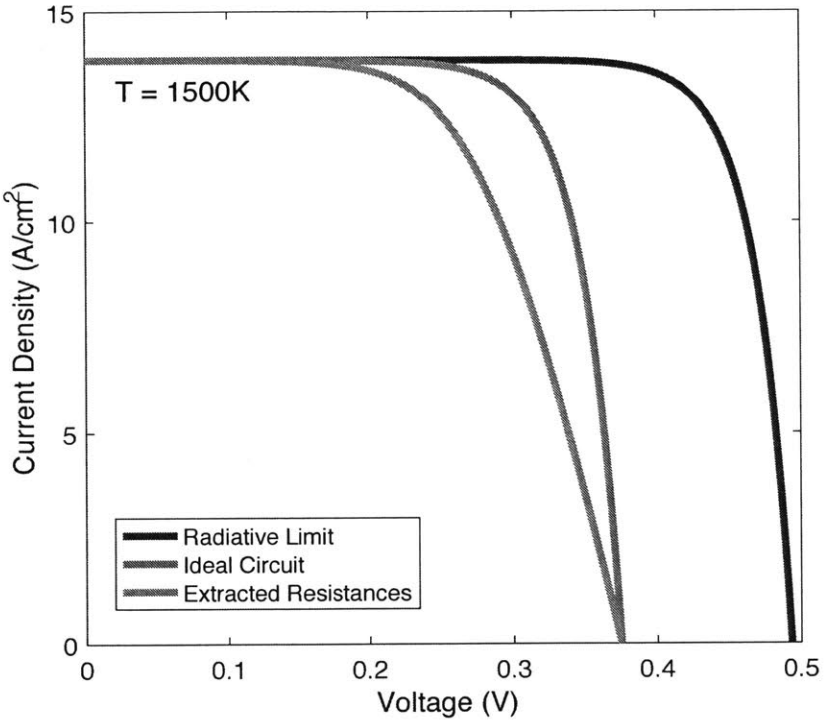

Figure 20: Current-voltage relationship for three representative conditions for the InGaAsSb cell, assuming a perfect blackbody emitter and unity IQE above the bandgap.

From these calculations, we determined that the best TPV efficiency we could achieve given all the previous considerations is 24.2%.

The remaining three losses come from: Non-unity view factor between the emitter and the PV cell surface, conduction heat loss through the supports, and parasitic absorption through the PDMS

epoxy that bonds the optical filter to the PV cell. The view factor between the emitter and the filter surface was high, ~98.5%. Given the filter thickness of 400 μm, the view factor between the emitter surface and the PV cell was closer to 95%. The supports were made from hypodermic stainless steel needles. A radiative fin analysis suggests that ~5-10% of total input heat was conducted through this channel. Lastly, the PDMS epoxy has ~5% absorption loss in the high-energy (i.e., transmitted) band. Together, these three losses represent about 25-30% loss in power and after taking them into account the efficiency drops down to 17.1%.

3.6 INCOMPLETE PHOTOTHERMAL CONVERSION

The next important consideration is coupling light into the TPV converter. A method for improving the efficiency by pushing the area ratio and therefore the optical concentration to high values has been demonstrated in our previous work[10], [11]. Our device takes advantage of blackbody absorption in our vertically aligned Multi-Walled Carbon Nanotubes (MW-CNTs) in a planar setup. However, as described in the references, high area ratios in a planar device begin to add higher levels of heat loss from the so-called "inactive" area.

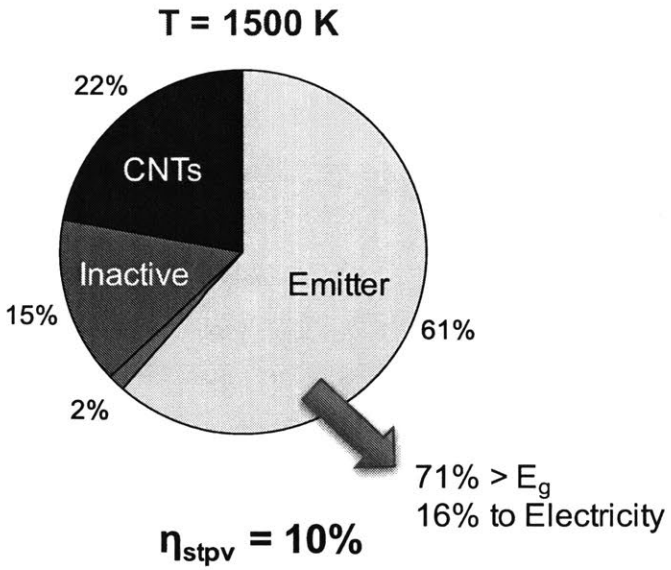

Figure 21: Breakdown of energy flow in our planar solar-TPV demonstration. The efficiency of 10% was not quite achieved due to a limited input power supply.

Even with area ratios between the emitter and absorber surfaces as high as 10, Figure 21 shows that still only ~65% of our energy goes to our TPV device and the rest is emitted from either the blackbody surface or the inactive surface. This effect limits the conversion of sunlight into electricity to ~10%. This is the highest efficiency that could have been recorded in our experimental setup provided all the loss mechanisms, both fundamental and non-fundamental. Instead, we reported an efficiency of 6.8%. We can see in Figure 22 that this experimental demonstration was limited in output power density, or emitter temperature. Had the temperature of the absorber/emitter device been increased, the model predicts that we would have demonstrated ~10% at an output power of 1 W/cm^2.

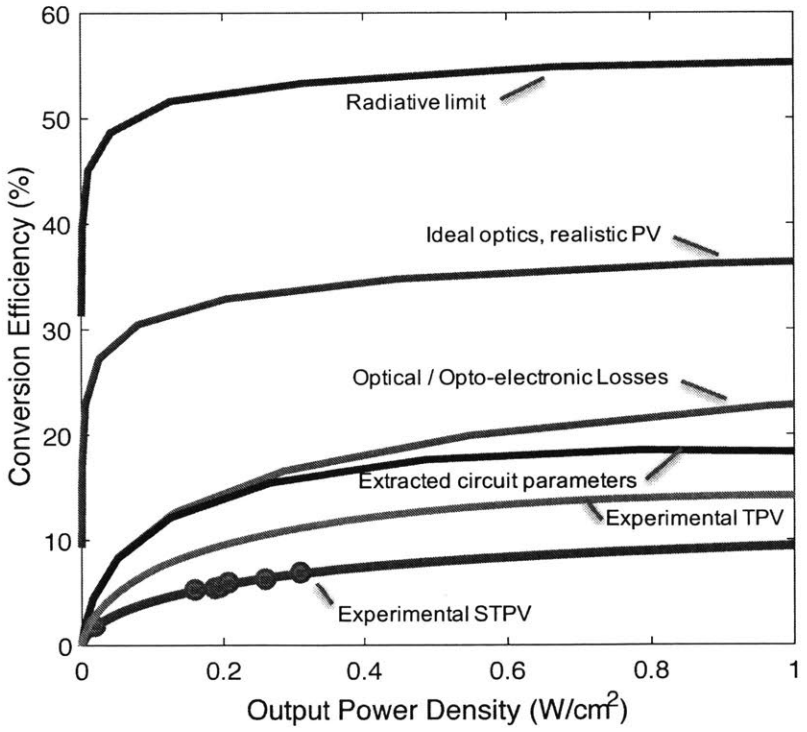

Figure 22: Conversion efficiency in the limiting cases that are described in this chapter as a function of output power density.

We have described a series of losses beginning with most fundamental and ending with most practical to explain the performance that we have reported in this thesis. Since a solar thermophotovoltaic device is necessarily a multi-disciplinary endeavor, quantifying these losses

in this way establishes a framework for a technology roadmap that can be used by researchers in different fields to understand where their expertise may contribute. A summary of this roadmap is shown in Figure 23.

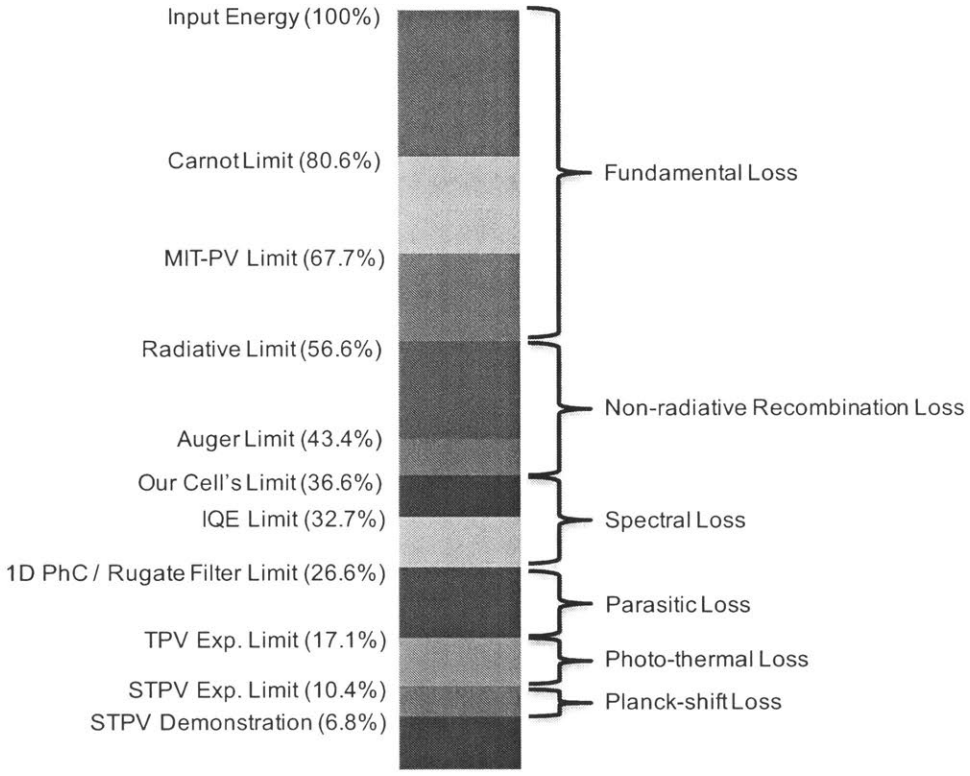

Figure 23: Summary of the loss mechanisms ranging from top down in order of most fundamental to least.

3.7 TOWARDS UNITY PHOTO-THERMAL CONVERSION

We propose a design that de-planarizes the energy flow of the solar-TPV device. By incorporating a blackbody cavity with a high aspect ratio, we can couple high optical powers into the *volume* of the device and rely on radial heat conduction to power the emission into the TPV converter[70].

This can be explained more clearly by looking at a simple energy balance to describe the heat transfer in the device:

$$A_{abs}CG_s = A_{abs}\sigma T^4 + A_{emit}\epsilon_{emit}\sigma T^4 + UA_{parasitic}T^x \tag{13}$$

where A_{abs} is the aperture area where light enters, C is the optical concentration, G_s is the solar constant of 1000 W/m^2, ϵ_{emit} is the hemispherical thermal emission from the emitter surface, $A_{parasitic}T^x$ represents a parasitic loss term that captures general conduction support losses. If we neglect support losses and rearrange this expression, we can re-write equation 13 to:

$$CG_s = \sigma T^4 + AR\epsilon_{emit}\sigma T^4 + \frac{A_{parasitic}T^x}{A_{abs}} \tag{14}$$

Equation 14 indicates that if we can establish large separation between the area of the emitter and area of the absorber, we can direct all of the energy to flow towards the emitter. For a blackbody cavity, the criteria to pass 50% of power to the emitter is $AR \gg 1/\epsilon_{emit}$. We can accomplish this level of AR through novel triangular cylindrical geometries. The triangular profile allows us to maintain planar (i.e., high) view factors with planar PV cells. A triangle was chosen as it maximizes the emitter surface area relative to the internal volume. This internal volume is where thermalization occurs and ultimately dictates the aperture area through which concentrated sunlight enters. Thus, the triangular design allows us to have the maximum AR for a given volumetric cavity absorber.

We developed an experimental setup to demonstrate this cavity effect and how it can be utilized in a solar thermophotovoltaic device for high levels of photothermal conversion rates. The experiment is shown in Figure 24. We fabricated two different cavity geometries by sintering milled Tungsten (*Ceramaterials*)

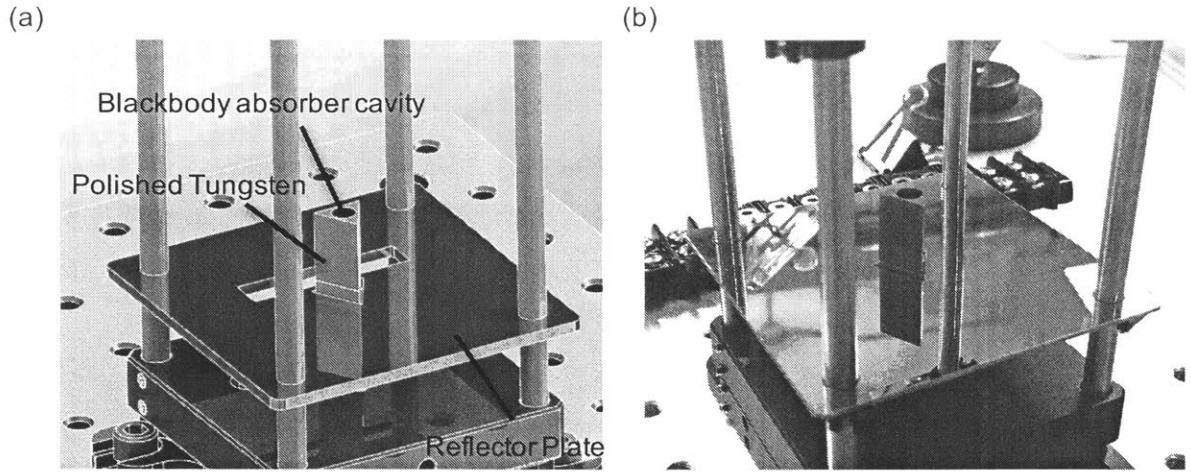

Figure 24: (a) Schematic showing the experimental setup to test increased photothermal efficiency with larger cavity sizes. (b) Optical image of the fabricated test setup.

This setup is put into a vacuum chamber and the pressure is reduced to less than 1 Pa, ensuring that the Knudsen number is >10 and we can effectively suppress other parasitic modes of heat transfer. We developed a laser diode system (*SAKAR Technologies*) that could couple high-intensity light into this vacuum chamber. Optical power through this laser is introduced to the blackbody cavity which raises the temperature of the system until quasi-steady state is established. This IR light source (wavelength of 919 nm) was chosen to replace the solar simulator in order to scale up the STPV demonstration without being limited by input power (as discussed in the previous chapter). This laser diode can allow us to input up to 200 W of optical power (>5000 suns) which can enable near unity photo-thermal conversion. Since we are taking advantage of blackbody absorbers, the spectral distribution of the incident light source is unimportant and all spectral information is lost upon thermalization within the cavity. To validate this assumption, a blackbody cavity's diffuse reflectance should be measured.

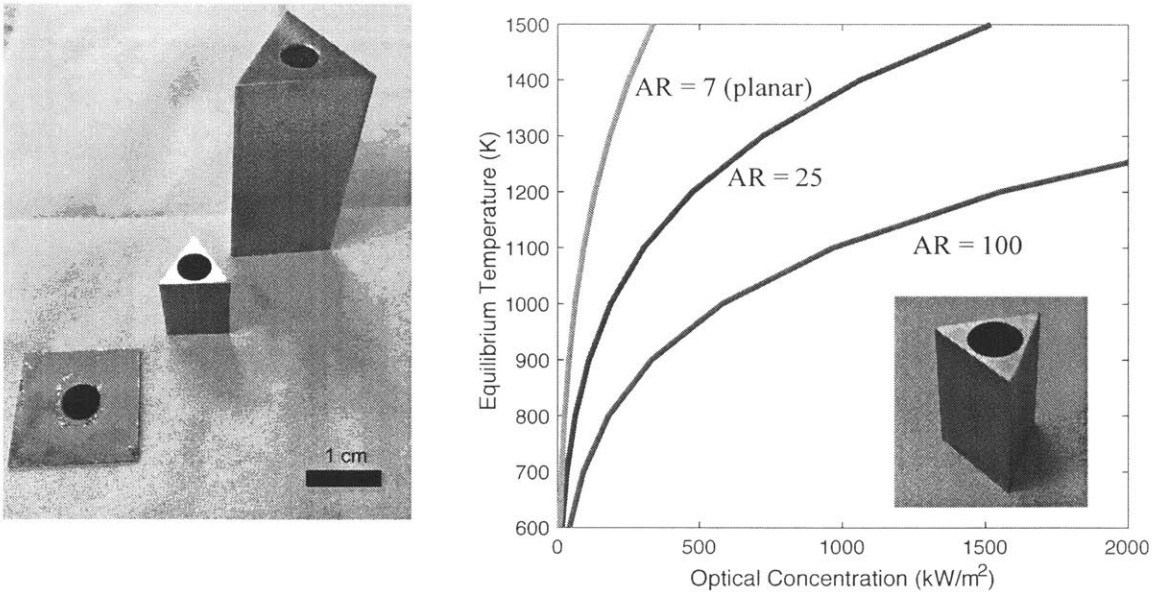

Figure 25: (a) Three different geometries tested in the photothermal experiment. (b) Quasi-steady state temperature as a function of input optical concentration for the three different cavities.

The solution to equation 13 is shown in Figure 25b. For a given optical concentration, high *AR* geometries yield lower equilibrium temperatures. While counter intuitive, it is this phenomenon that increases the photo-thermal conversion rate. Equation 13 shows us that the device which requires the highest optical concentration (i.e, input power flux) for a given temperature will be the most efficient. Future work will be carried out to fully characterize these devices by correlating the wall temperature (measured with a Type K thermocouple, assumed to be isothermal) with input optical power.

To understand how the integration of these cavities into a STPV system, we must consider the radiative heat transfer from the outer walls. We have slightly roughened the emitter surface to create a hemispherical emittance of ~0.3. This is approximately the effective emittance of the Si/SiO_2 photonic crystal / interference filter material set which was used for the previous STPV demonstration. Knowing this value, we may estimate the photo-thermal efficiency of the system by taking the ratio of emitted power to incident power. This is plotted in Figure 26.

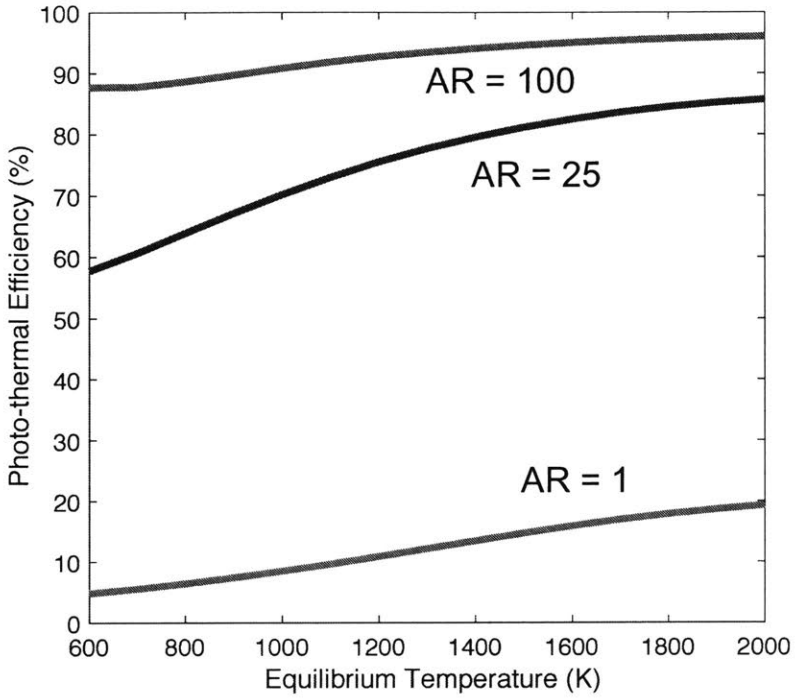

Figure 26: Estimated photothermal efficiency for the different geometries tested. Note that this efficiency is a strong function of the backside heat transfer rates.

It is important to note that the results in Figure 26 are system specific. In other words, the higher the emittance on the back-end is, the higher the photo-thermal efficiency, but the lower the TPV conversion rates. For example, pairing a blackbody emitter with a PV cell will ensure low TPV conversion but the photo-thermal efficiency will be relatively high (compared to a selective emitter). Thus, for a given emitter / PV pair, a cavity geometry should be selected to maximize overall efficiency given constraints in optical concentration.

We will use this concept and experimental setup to demonstrate that the incorporation of a blackbody cavity to a TPV converter can provide high (>90%) photothermal conversion rates if properly designed. If high enough optical concentrations can be achieved using 2-axis solutions such as heliostat fields or dish concentrators, this absorber loss can be considered negligible and the entire system efficiency will converge on the TPV efficiency.

Chapter 4

4. Thermodynamic Considerations of Spectral Splitting for High-Efficiency Solar Energy Conversion

4.1 INTRODUCTION

Solar spectral splitting is a strategy to optimize the extraction of exergy from sunlight through the separation of incident photons by their energy levels (or wavelengths). This approach generally implements any combination of thermal, electrical, or chemical processes that can increase the efficiency of a device[71].

Solar photothermal (*PT*) and photovoltaic (*PV*) conversion strategies each have their unique benefits and disadvantages, and the limiting efficiencies of both strategies have been discussed extensively[6], [17], [60], [72]. To take advantage of both technologies simultaneously, hybrid converters have been of great interest. The design of a number of these converters have been reported[73]–[76]. General methodologies for the optimization of these devices have been presented and used to compare different systems[77], [78] but the upper-bounds of performance for such strategies have not been determined.

Previous limiting efficiencies of *PT-PV* hybrid systems that split incident light into two bands (above and below bandgap) have been calculated and reported[79], [80]. Allowing for the thermalization of high-energy photons, however, by introducing a high-energy cutoff in the spectral splitter can vastly improve device performance by trading waste heat generation in the PV for useful power generation in the thermal collector.

Here we develop a methodology to understand the theoretical limits and optimum design of a hybrid *PT-PV* converter that includes both a high- and low-energy conversion cutoff. By investigating how the limiting efficiency is related to the spectral bandwidth illuminating the PV, we explain how the highest performing device indeed minimizes overall entropy generation by diverting *each* photon mode to the converter where it generates the least amount of entropy.

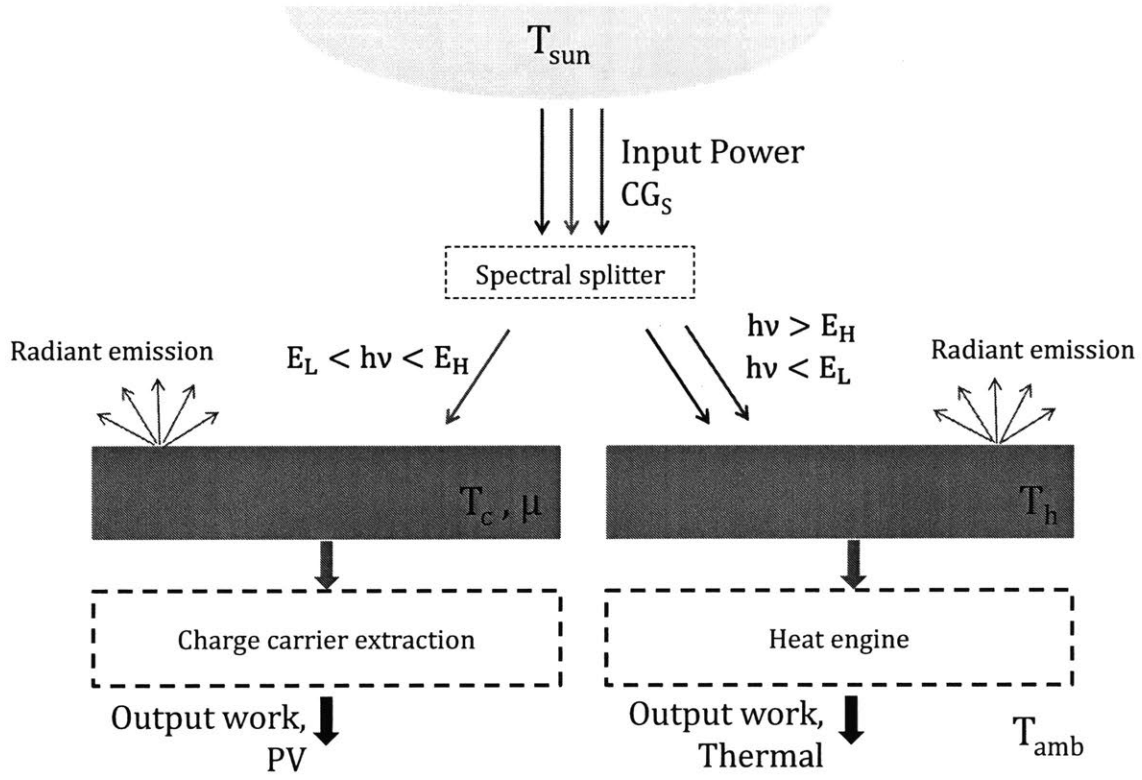

Figure 27: Thermally decoupled PV and PT operating in parallel which are powered by incident sunlight. The sunlight is separated based on its frequency into a PV band ($E_L < h\nu < E_H$) and a thermal band. Excited charge carriers are extracted from the PV at a potential, μ_c. Generated heat in the thermal absorber is converted to work through the temperature difference T_h-T_{amb}.

4.2 MODEL FORMULATION

Figure 27 depicts the general approach of the hybrid *PT-PV* converter, where a thermal engine and a photovoltaic cell sit in parallel under concentrated solar radiation. A key question that needs to be addressed when designing such a hybrid system based on spectral splitting is: To which converter should each incident photon mode be directed in order to reach the highest conversion efficiency? To understand the fundamentally limiting aspects of the conversion process in this device, an idealized hybrid system was studied. The spectral splitting concept considered in this study uses incident radiation which is distributed between the *PT* and *PV* converters via three bands, as described below. A blackbody source at T_{sun} = 5777 K (the thermodynamic temperature of the Sun[81]) generates a spectrum of electromagnetic radiation, denoted as G_s, which illuminates a lossless spectral splitter at an optical concentration, C. The splitter separates incident photons based on their frequency. Low energy photons ($h\nu < E_L$) and high energy photons

($h\nu > E_H$) are directed towards the thermal collector, where E_L and E_H represent the low and high energy levels of the *PV* band, respectively. The absorber surface of this collector is assumed to be ideally angularly and spectrally selective – it is only in radiative communication with the Sun. The net heat gained as a result of the interaction can be described by the difference between what is absorbed from the solar spectrum and what is emitted by the thermal collector. Since there are two different "thermal" spectral bands, this can be determined by calculating separate integrals:

$$Q_{net} = \int_{E_{cut}}^{E_L} [CG_s - \int_0^{\theta_s} Q_{BB}(T_H, h\nu)\, d\theta]\; d(h\nu) + \int_{E_H}^{E_\infty} [CG_s - \int_0^{\theta_s} Q_{BB}(T_H, h\nu)\, d\theta]\, d(h\nu) \quad (1)$$

where E_{cut} is the photon energy that maximizes the net heat generation (*i.e.,* the location of the transition between high absorption and low emission on the selective absorber surface), θ_s is the incident cone angle of the concentrated solar spectrum, E_∞ is the photon energy corresponding to the highest relevant energy in the system (~5 eV), and Q_{BB} is the blackbody spectrum characterized by T_H. This heat is then coupled to a reversible heat engine with a hot-side temperature equivalent to the absorber temperature and the cold-side temperature set at T_{amb} = 300 K. Thermodynamic work, W_{therm}, is extracted based on the Carnot efficiency between these two temperatures.

Meanwhile, photons that have energy within the designated spectral bandwidth (*i.e.*, $E_L < h\nu < E_h$) are directed towards a PV acting in the detailed balance limit. Note that if the spectral bandwidth were to span the entire solar spectrum, this model would recover the Shockley-Queisser efficiency limit[17] with the solar spectrum estimated as that of a blackbody at T_{sun}. Since sub-bandgap light is unconvertible regardless of its wavelength, we fixed E_L to the bandgap, E_g. Based on the constraints of our model (*i.e.*, $E_L = E_G$), incident radiative energy that illuminates the PV is all above the bandgap of the cell and therefore only interacts with a blackbody surface with an internal quantum efficiency (IQE) of unity. However, due to the applied voltage, radiative recombination is accounted for through the chemical potential, μ_c. Thus the generated photocurrent is given by:

$$I_{sc} = IQE \cdot q \int_{E_L}^{E_H} [CG_s - \int_0^{\theta_s} \frac{(h\nu)^2}{c^2} \frac{1}{exp\left(\frac{h\nu - \mu_c}{k_b T_c}\right) - 1} d\theta_s] \, d(h\nu) \quad (2)$$

where q is the elementary charge and k_b is the Boltzmann constant. The corresponding electrical energy that the cell may extract from these carriers can be determined by maximizing the product of I_{sc} and μ_c by varying the cell potential, μ_c:

$$W_{elec} = max\ (\mu_c \cdot I_{sc}(\mu_c)) \quad (3)$$

We determine the sum of the output work from the heat engine and the output work from the photovoltaic cell divided by the input power to the device in order to define the efficiency:

$$\eta_{total} = \frac{W_{therm} + W_{elec}}{\int_0^{\infty} CG_s d(h\nu)} \ x\ 100\% \quad (4)$$

The model requires three inputs to solve for the efficiency: 1) the illuminating optical concentration, C, 2) the temperature of the thermal collector (T_h), and 3) the p-n junction's electronic bandgap.

For a representative example, Figure 28a shows the efficiency of a device with a bandgap of E_g = 1.1 eV (such as that of a typical Si PV), a thermal collector temperature of T_h = 666 K (the dissociation temperature of one of the most common solar thermal heat transfer fluids, Therminol, VP-1[82]), and an optical concentration of C = 46,000x (the thermodynamic limit[81]). For this case, the thermodynamic limit for conversion efficiency is η_{max} = 59.82%. See Figure S1 for the limiting efficiencies given other optical concentrations and thermal collector temperatures.

The efficiency of the thermal collector remains relatively constant as the PV spectral bandwidth is increased (it decreases slightly as a result of lower illumination intensity). For narrow PV spectral bandwidths, the efficiency of converting photons within the PV is significantly higher than the heat engine, however, the power generated is small. As the bandwidth increases, the efficiency monotonically decreases due to increased thermalization losses within the cell. In the model, the PV is held at ambient temperature ($T_c = T_{amb}$) in order to maximize the PV performance. Thus, no

work may be extracted from the heat generated due to the thermalization of the excess energy of an absorbed photon. Because the total conversion efficiency is a weighted average of these two efficiencies, a maximum exists for the hybrid converter at a particular spectral bandwidth.

Figure 28b shows the total conversion efficiency as a function of bandgap values and E_H (note that the spectral width in Figure 28a is related to E_H through $\Delta\lambda = hc/(E_g - E_H)$). Similarly, there is a global maximum in performance for a particular set of operating conditions (*i.e.*, T_h and C). For the case of T_h = 666 K, this occurs at a bandgap of E_g = 1.4 eV and yields a value of 60.8%. Interestingly, this efficiency is only one absolute percentage point away from at E_g = 1.1 eV. This suggests that the result is relatively insensitive to the PV bandgap so long as the spectral bandwidth is appropriately chosen.

We also solved the model for the conditions where there is only a low-energy cutoff (i.e., all high energy photons are incident on the PV) in order to elucidate the benefit of including a high-energy cutoff. In all cases, the presence of a high-energy cutoff enhances the performance. However, for larger PV bandgaps, this effect is diminished. For bandgaps higher than 1.5 eV, the relative performance enhancement is less than 5% (Figure S2).

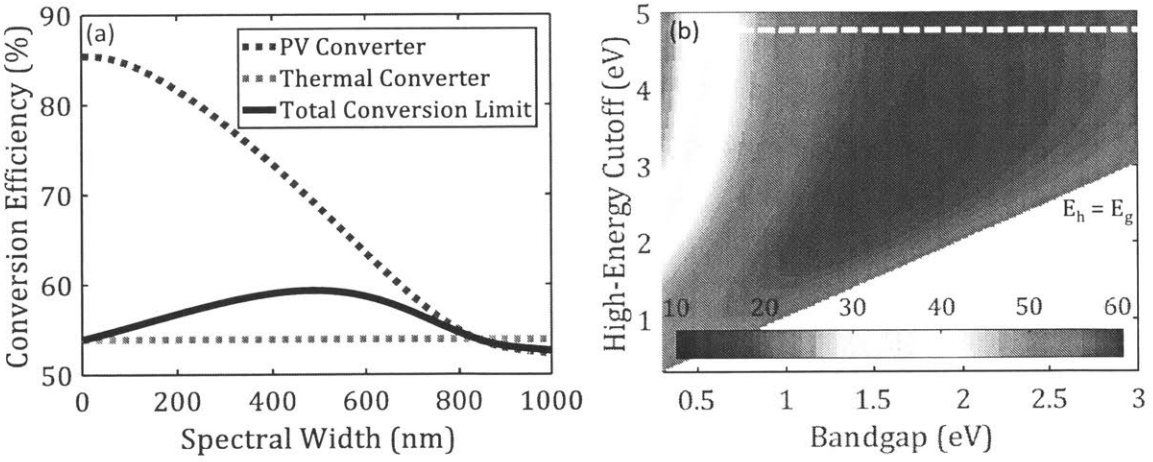

Figure 28: (a) Theoretical conversion efficiency limit for a hybrid PT / PV heat engine with a bandgap of E_g = 1.1 eV and a hot-side temperature of T_h = 666 K at full optical concentration. Also shown are the individual components of the total efficiency showing the nature of the optimum behavior. (b) Total conversion efficiency limit for a range of bandgaps and high energy cutoff (E_H) showing the presence of a global maximum given the thermal converter temperature,

T_h = 666 K, and input optical concentration, C = 46,000. 95% of the energy in the solar spectrum is below the white dashed line.

4.3 EFFECT OF TEMPERATURE AND OPTICAL CONCENTRATION

The limiting efficiencies presented with full solar illumination are far from achievable with present optical systems. Proposed hybrid systems are designed to operate closer to C = 100x. Figure 29a shows that the conversion efficiency slightly decreases as the optical concentration is reduced which is predominantly due to the decrease in chemical potential which has a logarithmic dependence on optical concentration (in the detailed balance limit). The dependence of the chemical potential on optical concentration is not substantial in this radiative limit and a relative decrease of about 10% of its value is observed for E_g = 1.1 eV across this illumination range.

A secondary effect of decreasing the optical concentration is that the decreasing chemical potential decreases the optimum spectral width, which further decreases the chemical potential. Figure 29 shows more information on how the chemical potential is affected by optical concentration. Additional efficiency losses may be attributed to a decrease in the photo-thermal efficiency. Since the loss in chemical potential is more detrimental than the decrease in relative heat gain at the hot absorber surface, we observe that the optimum spectral bandwidth shrinks as a result of decreasing optical concentration and a larger portion (~65%) of the output exergy is generated from the thermal collector.

Another way to decrease the optimal spectral bandwidth, but fundamentally increase the overall converter's efficiency is to increase the hot-side temperature. Figure 29b shows the effect of raising the heat-engine temperature from 573 K to 2544 K. This behavior occurs until the hot-side temperature reaches 2544 K and the optimum spectral bandwidth is reduced to 0. At this point, the model has reduced to the Blackbody limit for solar energy conversion[72]. Modulating the hot-side temperature can effectively tune the portion of exergy derived from the heat engine.

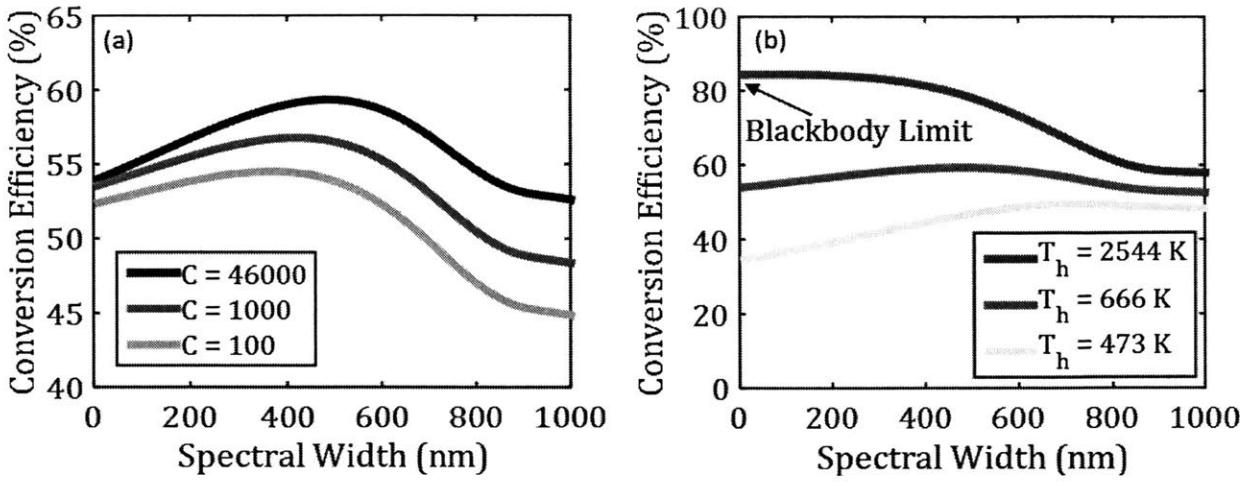

Figure 29: (a) Effect of decreasing optical concentration on the overall conversion efficiency and the optimum spectral bandwidth. Both the shrinking of the bandwidth and decreasing the efficiency are a result of the decreased PV voltage. (b) Effect of increasing the hot-side temperature, T_h which increases the overall conversion efficiency and shrinks the optimum spectral bandwidth due to the increase of the heat engine efficiency. In both figures, $E_g = 1.1$ eV.

4.4 PERFORMANCE IMPROVEMENT ASSOCIATED WITH INCLUSION OF HIGH-ENERGY CUTOFF

Another important consideration is whether or not the high-energy cutoff is necessary. As has been shown and heavily studied, the presence of the low-energy cutoff (i.e., sub-bandgap photon utilization) can increase the efficiency of the system dramatically. In fact, the effect of including a high-energy cutoff to send high-energy photons to the thermal collector instead of the PV is also beneficial to the overall conversion efficiency of a hybrid device. Figure 30, however, shows the diminishing effects of this high-energy cutoff as the bandgap increases. At 2 eV, the benefit of including the high-energy cutoff has practically vanished as only about 35% of incoming solar energy is above this value. For $E_g = 1.1$ eV (such as that of Si), relative theoretical enhancements of ~15% may be achieved by incorporating a high-energy cutoff at these thermal collector temperatures. Additionally, as the heat engine temperature, T_H, increases for a given bandgap, the relative improvement the hybrid system can provide begins to vanish.

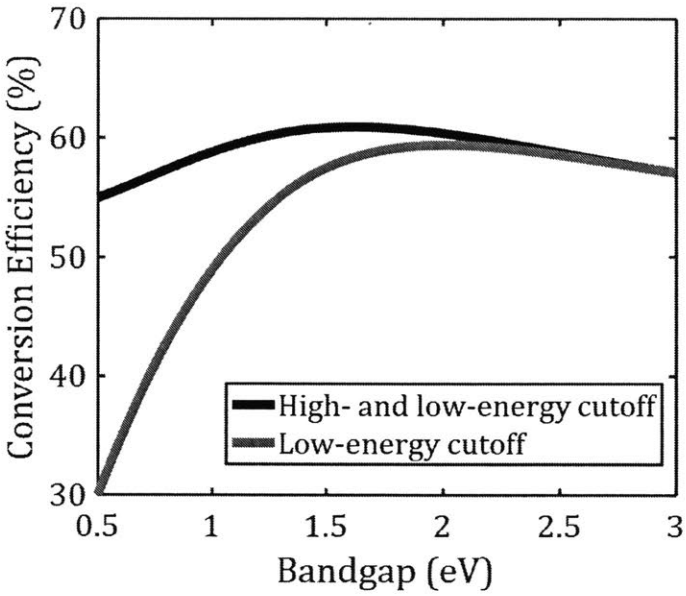

Figure 30: Performance of the optimized hybrid system with a high- and low-energy cutoff compared to that of a single cutoff (at the bandgap, E_g) hybrid converter for T_H = 666 K. The enhancement in overall conversion efficiency with the inclusion of a high energy cutoff diminishes with increasing PV bandgap.

4.5 THE VALUE OF THE CHEMICAL POTENTIAL RELATIVE TO THE CELL BANDGAP

In the detailed balance limit, the chemical potential is determined by maximizing the product of the generated photocurrent (a function of the chemical potential due to radiative recombination) and the chemical potential. In this limit, the higher the carrier generation rate, the higher the ratio of chemical potential (μ_c) to bandgap energy (E_g).

InFigure 31, the effect of optical concentration on the operating chemical potential is presented. For lower optical concentrations, using $\mu_c = E_g$ will tend to overestimate the optimum bandwidth. This can be corrected by applying a more accurate value for μ_c which can be either calculated using the detailed balance or empirically determined for an actual cell that may exhibit other dominant recombination mechanisms.

Figure 31b shows this ratio as a function of optical concentration for a few relevant bandgap values at the optimum spectral bandwidth. The logarithmic dependence of μ_c with concentration implies that small

differences in illumination will have little effect on the estimation of the optimum window (via Equation (14) or (15)) unless there are differences in order of magnitude.

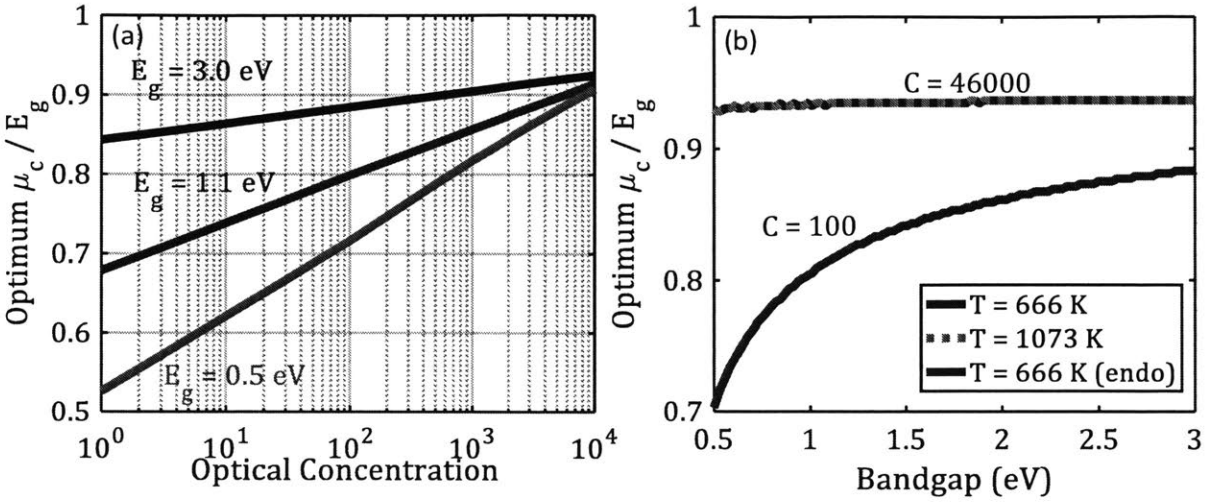

Figure 31: (a) Ratio of chemical potential, μ_c, to bandgap energy, E_g, for the entire range of possible optical concentrations for the optimum spectral bandwidth. In the radiative limit, there is a logarithmic dependence suggesting that the variation in this ratio is only relevant when changing illumination levels by orders of magnitude. (b) Ratio of μ_c to E_g for the optimum spectral bandwidth as a function of E_g shown for the cases corresponding to those discussed later in the chapter.

4.6 ENTROPY GAIN OF THERMODYNAMIC SYSTEM

To properly describe the three spectral bands for the spectral splitter (*i.e.*, PT_{high} ($>E_H$), PV, and PT_{low} ($<E_L$)), the entropy increase of the system for a given photon mode interacting with either the PV or the thermal collector is considered. The general form for a photon's entropy is given in [83]:

$$\delta S_{photon} = \frac{h\nu - \mu_c}{T_c} - k\left[\exp\left(\frac{h\nu - \mu_c}{kT_c}\right) - 1\right]\ln\left[1 - exp\left(-\frac{h\nu - \mu_c}{kT_c}\right)\right] \quad (5)$$

Given the operating principle of the PV, some amount of work, μ_c, can be extracted. Note that μ_c only has physical significance for photon energies above the bandgap, E_g. In the limit of open-circuit operation, the excess energy, $h\nu - \mu_c$, would exist as heat that is rejected at T_c.
From Equation 5, in the limit where $h\nu - \mu_c \gg kT_c$:

$$\delta S_{PV} = \frac{\delta Q}{T_c} = \frac{h\nu - \mu_c}{T_c} \tag{6}$$

The incremental entropy increase based on the exchange in the open-circuit limit is therefore, the difference between these two values:

$$\delta S_{gen,PV} = \delta S_{PV} = \frac{h\nu - \mu_c}{T_c} \tag{7}$$

For the thermal collector, there is no chemical potential since the interactions give rise to thermal excitations. The spectrally dependent entropy increase for the photo-thermal interaction can be written similarly as:

$$\delta S_{gen,PT} = \delta S_{PT} = \frac{h\nu}{T_h} \tag{8}$$

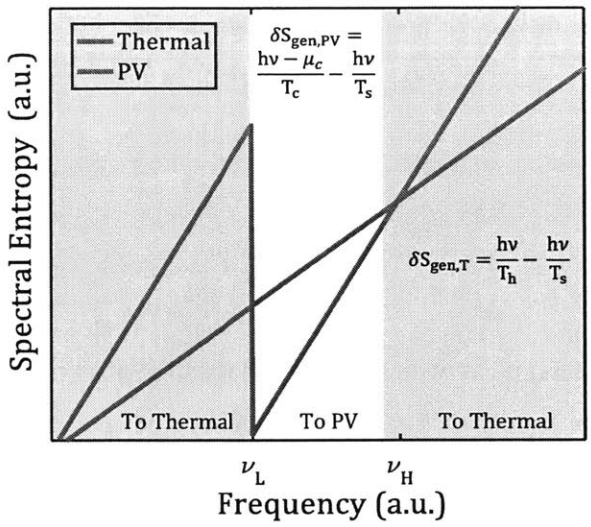

Figure 32: Spectral entropy generation for a particular photon frequency as it interacts with either the thermal or PV system. The ultimate strategy for entropy minimization is to choose, for a particular frequency, the interaction which generates the least entropy. This gives rise to three distinct bands separated by the two cross-over values.

Figure 32 shows the $\delta S_{gen,PV}$ and $\delta S_{gen,PT}$ with respect to the photon frequency. $\delta S_{gen,PV}$ takes on a piecewise function based on the step change in the chemical potential, μ_c, *i.e.*, because the bandgap energy represents an abrupt change between the ability and inability to extract work from a photon. A constant chemical potential with a value of E_g is assumed here. In reality, the operating chemical potential will be lower than E_g due to recombination effects, but in the detailed balanced limit at full optical concentration, it is within 10%. For lower optical concentrations, using $\mu_c = E_g$ will tend to overestimate the optimum bandwidth. This can be corrected by applying a more accurate value for μ_c which can be either calculated using the detailed balance (Figure S3) or empirically determined for an actual cell that may exhibit other dominant recombination mechanisms.

The functional form of $\delta S_{gen,PV}$ in Figure 32 is critical to the design of the spectral bandwidth as it implies that there are exactly two crossovers with the linear function of $\delta S_{gen,PT}$. These crossover points determine, for a particular frequency, where one interaction (i.e., solar-thermal or solar-PV) becomes more favorable compared to the other from an entropy generation perspective. The low-energy crossover occurs when μ_c assumes a finite value (i.e., the bandgap of the PV, E_g). This is to be expected, since the PV converter has a frequency dependent response and is most sensitive

to incident light at energies just at or above its bandgap. The high-energy crossover can be determined by setting $\delta S_{gen,PV}$ equal to $\delta S_{gen,\,PT}$ and solving for the corresponding $h\nu_H = E_H$. This occurs when:

$$h\nu_H = E_H = \frac{\mu_c}{1 - T_c/T_h} \tag{9}$$

E_H physically represents the point at which the thermalization loss in the PV overcomes the chemical potential gain. Thus, purely thermal conversion becomes preferable.

The limiting efficiencies presented with full solar illumination are far from achievable with present optical systems. Proposed hybrid systems are designed to operate closer to C = 100x. Figure S3a shows that the conversion efficiency slightly decreases as the optical concentration is reduced which is predominantly due to the decrease in chemical potential which has a logarithmic dependence on optical concentration (in the detailed balance limit). The dependence of the chemical potential on optical concentration is not substantial in this radiative limit and a relative decrease of about 10% of its value is observed for E_g = 1.1 eV across this illumination range.

4.7 ENTROPY-BASED SYSTEM OPTIMIZATION

By integrating over the entire spectrum of interest, the total entropy generation, S_{gen} can be evaluated as a function of the high-energy cutoff, E_H:

$$S_{gen} = \int_{E_{cut}}^{E_L} \frac{h\nu}{T_h} - \frac{h\nu}{T_{sun}} d(h\nu) + \int_{E_L}^{E_H} \frac{h\nu - \mu_c}{T_c} - \frac{h\nu}{T_{sun}} d(h\nu) + \int_{E_H}^{E_\infty} \frac{h\nu}{T_h} - \frac{h\nu}{T_{sun}} d(h\nu) \tag{10}$$

$$S_{gen} = \frac{1}{2}\left[\left(\frac{1}{T_h} - \frac{1}{T_{sun}}\right)(E_L^2 + E_\infty^2 - E_H^2) + \left(\frac{1}{T_c} - \frac{1}{T_{sun}}\right)(E_H^2 - E_L^2)\right] + \frac{\mu_C}{T_c}(E_L - E_H) \tag{11}$$

Thus:

$$\frac{\partial(S_{gen})}{\partial(E_H)} = 0 = E_H\left(\frac{1}{T_c} - \frac{1}{T_h}\right) - \frac{\mu_c}{T_c} \tag{12}$$

and it indeed exhibits a minimum value when E_H is equal to $\frac{\mu_c}{1-T_c T_h^{-1}}$, the second crossover point of the functions $\delta S_{gen,PV}$ and $\delta S_{gen,PT}$. The efficiency, as calculated from the previously discussed thermodynamic model is shown in Figure 4a for two arbitrary bandgaps (Eg=1.1 and 2.0 eV) as a function of E_H. The corresponding S_{gen} (Equation 11) is shown in Figure 33b. The point of minimum entropy generation as a result of the spectral interactions as described by Equations (7) and (8) corresponds to the point of maximum exergy extraction (and thus conversion efficiency). Thus, the spectral bands that maximize exergy output can be determined by investigating a particular photon mode and its interaction with a particular converter (thermal or PV), and simply choosing one which generates the least entropy.

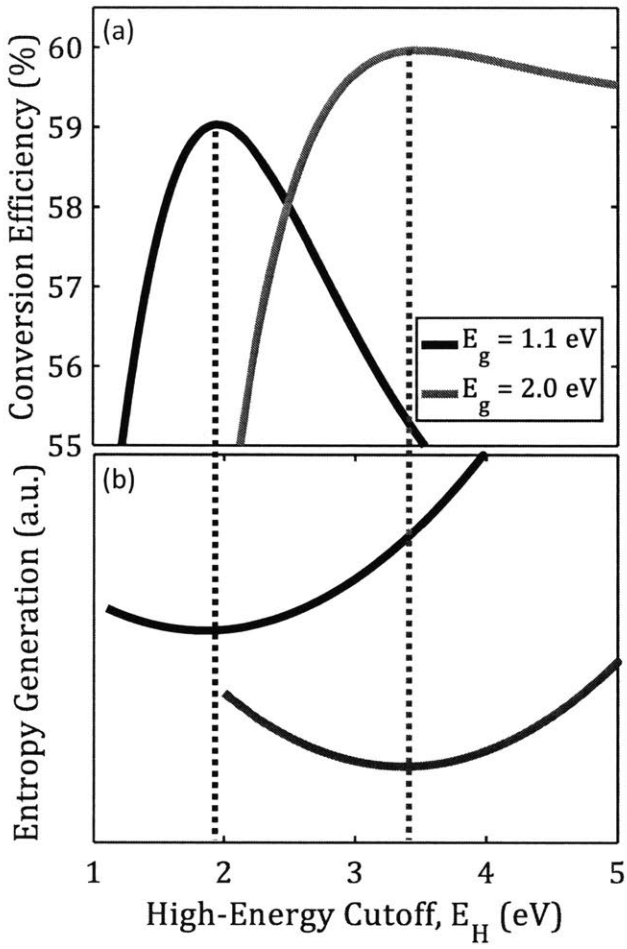

Figure 33: (a) Total conversion efficiency limit from the system-level model for two arbitrary bandgaps at a converter temperature of $T_H = 666$ K and full optical concentration.(b) The function S_{gen} plotted for the same two bandgaps exhibiting a minimum at a spectral bandwidth corresponding to the maximum exergy in the system-level model. Additionally, a lower absolute entropy generation corresponds to a higher exergy production.

This analysis can be extended to any number of hybrid converters to determine the proper spectral bands for maximum energy conversion efficiency. The optimum high-energy level, E_H, in the ideal case is a ratio of the chemical potential of the PV to the reversible conversion efficiency of the heat engine when the PV temperature, T_c, approaches the ambient temperature, T_{amb}. For more practical operation, the heat engine is more likely to operate near the endo-reversible thermodynamic limit[84] (*i.e.*, *Curzon* & Ahlborn engine). Following the method previously

described, but including the irreversibility of the heat engine, one can derive the cutoff for more practical operation corresponding to the maximum output power:

$$E_{H,NE} \approx \frac{\mu_c}{\left(1-\sqrt{\frac{T_c}{T_H}}\right)} \tag{13}$$

Equations (12) and (13) provide a measure of the *quality* of the PV relative to the thermal converter but show no apparent dependence on the incident light spectrum. However, energy conservation needs to be verified before implementation (*i.e.*, T_H could never be greater than T_{sun}). Additionally, for values of E_H greater than ~5 eV, the estimate breaks down since <1% of the energy of the solar spectrum is above this value and the high-energy cutoff becomes irrelevant.

The efficiency limits for both the ideal hybrid converter at full concentration (the thermodynamic limit) and the endoreversible hybrid converter operating under an optical concentration of 100x are shown in Figure 5a. The top curve represents the best possible terrestrial performance for a hybrid *PT-PV* system while the bottom curve represents the best possible performance given more realistic operating conditions, *i.e.*, all non-essential entropy generation is suppressed.

The agreement between the entropy minimization model and the system-level model for predicting the optimum bandwidth is shown in Figure 5b through a range of E_g and hot-side temperatures for both ideal and non-ideal cases. This good agreement suggests that without knowledge of the efficiency via a detailed system model, the spectral bandwidth that corresponds to the maximum system performance and over which photon energies that bandwidth should be applied is known. Further modifications can be made to Equation (13) such as a reduction of μ_c in order to account for non-idealities such as non-radiative recombination. This can be a powerful tool to approximate the optimum design for actual systems. It can aid the choice of photonic design and material set, revealing important length-scales and spectral regions.

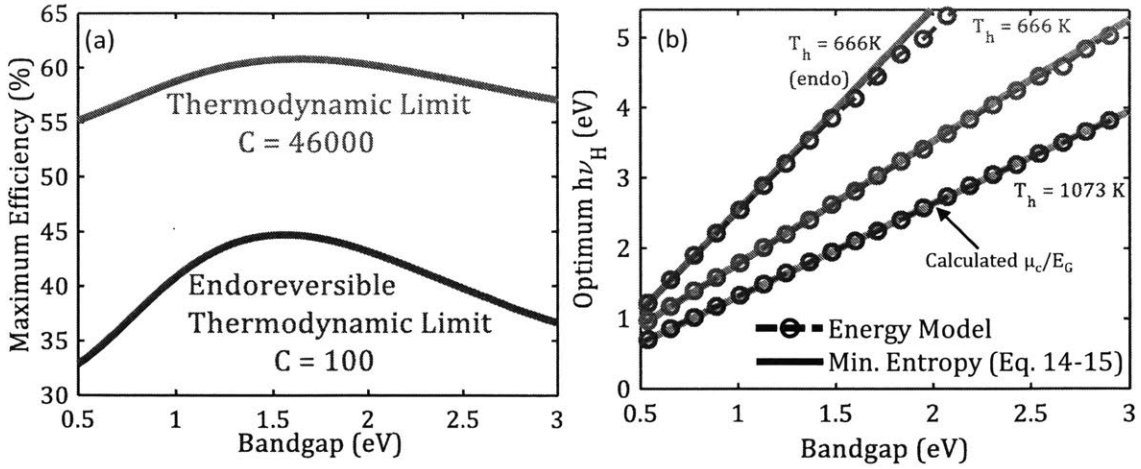

Figure 34: (a) The efficiency limits for the spectral splitting hybrid converter as a function of bandgap in both the reversible and endoreversible case for a hot-side temperature, $T_H = 666$ K. (b) A comparison of the optimum E_H calculated from the system-level model at maximum efficiency and the entropy generation model at minimum S_{gen}. The two models show excellent agreement within a wide range of relevant bandgaps and temperatures.

4.8 CONCLUSIONS

We have presented the thermodynamic limits of a hybrid solar power generation device composed of a photovoltaic cell and a thermal engine in parallel. We provide a simple method for determining the optimum spectral bandwidth of an optical splitting element in this device based on a frequency-dependent entropy minimization scheme. In fact, the exact spectral bands that maximize exergy output can be determined by considering the interaction of a particular photon mode with a particular converter, and choosing the option that generates the least entropy. The optimal spectral window to the PV is inversely proportional to the heat engine efficiency and scales linearly with the bandgap of the PV. We showed that the inclusion of a high-energy cutoff always enhances the theoretical performance relative to a single, low-energy cutoff, although at diminishing returns for higher PV bandgaps. This concept is extended to non-ideal systems and we show that with proper modifications, more realistic systems can be understood using this spectral entropy minimization technique in order to increase the usefulness of the analysis.

Chapter 5

5. Thermal Radiative Runaway in Ultra-thin Vanadium Dioxide Structures

5.1 INTRODUCTION

Uncontrolled positive feedback in thermal systems leads to a well-known phenomenon called thermal runaway. Broadly speaking, thermal runaway occurs when a rise in system temperature leads to an event that promotes a further increase in its temperature. This behavior has been observed and well-studied in many different physical sciences such as exothermic chemical reactions [85], [86], nuclear fusion reactions [87], [88], semiconductors [89], [90], two-phase thermal fluid systems [91], [92], microwave radiative pumping of ceramics [93], [94] and atmospheric chemistry [95].

In thermal radiation, a thermal runaway is observable in a system that exhibits negative differential emittance (NDE) when a constant heat flux is applied. NDE is a thermal phenomenon in which increasing the surface temperature decreases the heat flux that is radiated from the surface. If the amount of heat applied is fixed, then an NDE system trying to find a steady state could undergo a large increase in surface temperature, as the excess amount of heat is driven into the capacity of the system until equilibrium is reached. Materials that have thermally induced insulator-to-metal phase changes[96] (IMT) are prime candidates to demonstrate this thermal runaway phenomenon, as their optical properties can vary drastically over a small temperature range.

Vanadium oxide (VO_2) is a long-studied correlated electron material that transitions from an insulator to a metal near room temperature (~340 K)[97], [98]. The IMT is accompanied by a change in the lattice structure as the material moves from a monoclinic to a tetragonal structure. Delaire *et al.*[99] discussed the role of anharmonic (high entropy) phonons in driving the switch between competing phases. Because of this transition, as the temperature of the surface increases past the critical temperature, the thermal emittance can have a large and abrupt change from a high to low value [98], [100], [101]. This reduction in emittance may be enhanced by increasing the

low-temperature (insulator) emittance in the spectral region where the photon population of the emitter is maximized before the phase change. This has been demonstrated by Kats *et al.*[101], taking advantage of the lossy dielectric properties of the VO_2 on a sapphire substrate. While NDE was predicted for this structure, it has never directly been experimentally demonstrated. In this work, we use the concept of thermal runaway to provide direct experimental evidence of broadband NDE. The control and understanding of NDE has important implications for improving the sensitivity of a variety of devices.

5.2 CRITERIA FOR NEGATIVE DIFFERENTIAL EMISSION

The heat flux, defined as the heat loss per unit area, due to thermal radiation is well described by the Stefan-Boltzmann law,

$$Q''(T) = \bar{\varepsilon}(T)\sigma T^4 \tag{1}$$

where $\bar{\varepsilon}$ is the total spectral and hemispherical emittance from a surface, σ is the Stefan-Boltzmann constant, and T is the thermodynamic temperature in an absolute scale. The proper criterion for NDE can be determined by differentiating Equation (1),

$$\frac{dQ''(T)}{dT} = 4\bar{\varepsilon}(T)\sigma T^3 + \sigma T^4 \frac{d\varepsilon(T)}{dT} \tag{2}$$

In order to decrease Q'' by increasing T,

$$\left|\frac{d\varepsilon(T)}{dT}\right| > \frac{4\varepsilon}{T} \tag{3}$$

which is the criterion for NDE to be possible in the far-field. As suggested by Equation 3, simply decreasing surface emittance with increasing temperature is not a sufficient characteristic of a surface to exhibit NDE. Note that the required differential of emittance with temperature gets smaller with increasing temperatures, as incremental changes in the fourth power of temperature are less significant than changes in emittance (which could be changing by an order of magnitude).

At lower temperatures, however, perturbations in the fourth power of temperature are comparable to changes in emittance and NDE becomes much more difficult to achieve (*i.e.*, high $d\varepsilon/dT$ necessary).

For VO_2, the change from an insulator to a metal occurs at ~340 K. Assuming the surface emittance at that temperature is unity (an upper bound), the rate of change of emittance with temperature must be larger than ~0.01 K^{-1}. Past work which characterized the change in total emittance of engineered VO_2 [101], $|d\varepsilon/dT|$ can be as steep as 0.05 K^{-1}, making this surface a good candidate to study NDE and thus to demonstrate thermal runaway by exploiting mid-infrared radiation based on the temperature of the transition.

5.3 EXPERIMENTAL DEMONSTRATION

To create the VO_2 samples for the experiments, we first grew an epitaxial VO_2 film (150 nm thick) on a polished single crystal c-plane sapphire substrate using RF-magnetron sputtering using a V_2O_5 target (99.9% purity, AJA International Inc.). The substrate was held at 550 °C during film growth with an RF source gun power of 125 W. We flowed 99.50 sccm of Ar and 0.5 sccm of O_2 as the sputtering gas mixture to keep the chamber pressure at 10 mTorr.

We then designed a quantitative experiment to demonstrate how this VO_2 sample behaves when a controlled radiative heat flux is dissipated at its surface. Electrical current passed through a resistive Kapton heater that was sandwiched between two sapphire substrates with our thin-film VO_2 structure deposited on the polished outside surfaces. The conduction through the thermocouple and heater electrical leads was determined to be negligible compared to the radiative emission loss (<5%). Therefore we assumed that the electrical power dissipated in the device was equivalent to the total thermal radiation that was emitted from the structure (active VO_2 surface + inactive emitting surfaces).

The VO_2 / heater stack was placed into a vacuum chamber in close proximity to an IR-transparent viewport where we visualized the heating process with an IR camera in the 3-5 μm range. The chamber was evacuated to 0.1 Pa where the heat loss by conduction from the heated surface was much smaller than that of the thermal radiation ($Kn \sim 10^{-5}$). A step-change in voltage was applied

to the heater and the time-response of the temperature and IR signal was monitored. Steady-state was determined when variations in the temperature measurement were within the uncertainty of the thermocouple (~0.1 K).

In Figure 35a, the sample temperature initially increased with roughly a quartic behavior as the electrical power (i.e., radiative heat flux) delivered to the heater increased, according to Equation 1. However, at a heater power of ~0.495 W (a broadband radiative heat flux of ~330 W/m^2), the VO_2 film began to change phase, resulting in a NDE. Since the dissipated power remained constant, instead of NDE, we observed a thermal runaway (i.e., a jump in temperature) until the structure could reach thermal equilibrium at a fully metallic state. The heater temperature increased by ~15°C as a result of the newly metallic boundary condition. Also shown in Figure 35a is the radiative heat flux associated with blackbody emission at the given temperature. A similar phenomenon, as well as a hysteretic effect was observed while reducing the applied heat flux (cooling), which is well-explained in [102].

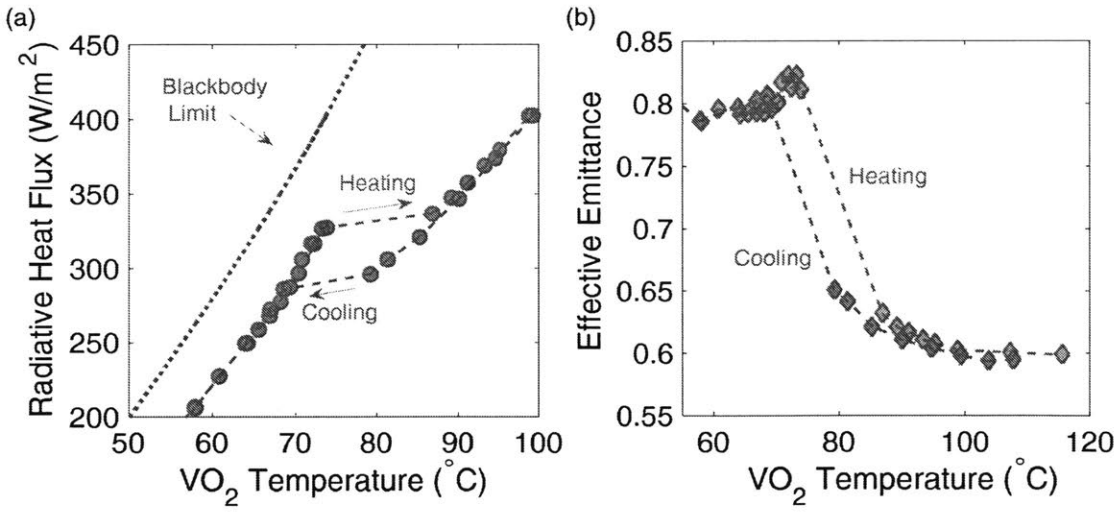

Figure 35: (a) The heating and cooling dynamics of a thin-film VO_2 emitter structure which underwent an insulator to metal transition. The thermal runaway, characterized by a ~15 K jump in temperature is attributed to an abrupt reduction in the emittance of the surface. (b) Effective emittance (ratio of measured heat flux to that of a blackbody) of the experimental setup. It represents a weighted average between inactive and active emission area.

Figure 35b shows the effective emittance -- the normalized radiative heat flux relative to that of a blackbody – for the VO_2 film. This represents a weighted average of emission between the inactive (sides, supports, etc.) and active (VO_2 film) emission area. The total emittance for both heating and cooling exhibits an enhancement beginning at ~70 °C at the target wavelength of 10 μm, before an abrupt change to metallic properties over a ~20 °C window. The emission remains higher at a given temperature during the transition for heating relative to cooling due to its predominantly insulator properties. Figure 35b shows a $|d\varepsilon/dT|$ of ~ 0.014 K^{-1} and thus NDE is observable according to the previously discussed criteria.

Figure 36a shows the time-response before, during, and after the IMT. The sample temperature first reached above 70 °C (blue line) when the input power was stepped up from 462 mW to 478 mW (red line). A first-order response was observed with a fitted time constant of 4.44 minutes, corresponding to the radiation loss from the VO_2 in its insulating phase. When the input power was again increased from 478 mW to 493 mW, the sample began to heat up with the same dynamics until it reached an inflection point, where the average emittance began to decrease sharply (~0.014 K^{-1}). While the sample reduced its emittance, the system had still not reached steady state and it continued to heat up, now with new time constant associated with the change in optical properties. This time constant corresponds to a lower heat transfer coefficient at the boundary (determined by the radiation from the metallic state). This time constant was quantified just above the transition when the power is again stepped from 493 mW to 507 mW. The fitted time constant was 7.10 minutes, an increase of ~59% relative to the insulating phase, which indicates that the system dynamics were heavily influenced by the VO_2 surface.

Data from IR imaging of the device during the heating experiment shows direct evidence of NDE as the cause of the thermal runaway (Figure 36b). The IR images from six representative data points in Figure 36c show that the emissive power decreases while the temperature monotonically increases.

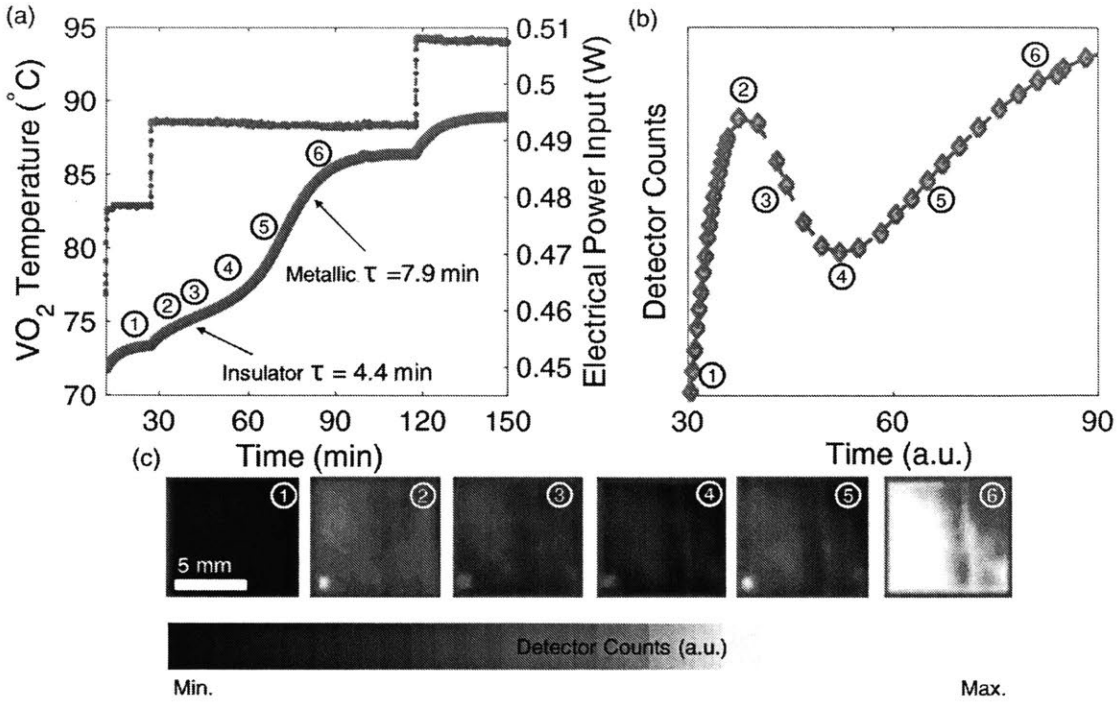

Figure 36: (a) VO_2 temperature plotted as a function of time before, during, and after the transition. On the secondary axis shows the applied heater power that is to be dissipated through the structure. (b) Average IR signal from the VO_2 surface during the transition. (c) IR images corresponding to the states 1-6 as denoted in the figures.

5.4 HEAT TRANSFER MODEL

To describe the dynamics of the experiment, we constructed a lumped thermal capacitance model with a temperature dependent emittance extracted from [17],

$$C\frac{dT}{dt} = Q_{in} - \bar{\varepsilon}_{ia}A_{ia}\sigma(T^4 - T_\infty^4) - \bar{\varepsilon}_{vo_2}(T)A_a\sigma(T^4 - T_\infty^4) \quad (4)$$

where C is the heat capacity of the system (determined experimentally), Q_{in} is the input heat (measured), $\bar{\varepsilon}_{ia}$ is the emittance of the non-VO_2 surfaces (assumed to be black), A is the area where the subscripts *ia* and *a* stand for inactive and active areas, respectively.

Figure 37a shows the results of this model, and is in good agreement with our experiments. It accurately predicts both the insulating and metallic time constants, as well as the steady-state temperature of the system. The total radiative heat loss leaving the system (Figure 37b) highlights the nature of the NDE demonstrated in our experiment. Based on the total optical properties of the system, a critical heat flux (CHF, Q_{crit}) corresponding to ~330 W/m^2 (~0.49 W of input power) is defined, which when surpassed, forces the system to its metallic state before equilibrium can be established. It is defined as the maximum possible radiative heat flux that can be supported by a surface with NDE properties without triggering thermal runaway. As described by Equation 4, this heat flow is comprised of both the active (from VO_2) and inactive (from sides, leads, etc.) component (inset of Figure 37b). Over ~50% of the power is lost through the inactive area which tends to suppress the NDE phenomenon since these losses have no negative temperature dependence.

We then used the model to study a pure VO_2 system (i.e., inactive loss of 0%) to investigate the most drastic thermal runaway possible given the optical properties of our thin-film VO_2 sample (Figure 37c,d). This was found by minimizing the thickness of the sapphire substrate to reduce the thermal mass. The minimum substrate thickness without significantly affecting the emission properties of the thin-film VO_2 is on the order of the penetration depth of sapphire (1 μm at the peak emittance wavelength [101]). At Q_{crit}, the system equilibrates at 74°C in an insulating phase, shown as a horizontal blue line in Figure 37c. However, when an additional incremental flux is supplied (i.e., <1% of Q_{crit}), the system is forced to its metallic state through a thermal runaway process. The minimum characteristic switching time is ~1.5 seconds for a minimum temperature rise of ~35°C. Increasing the "over-potential", or percentage of Q_{crit}, above the phase change allows for the tuning of the switching onset, but not the characteristic switching time, which is determined by the metallic optical properties and the thermal mass. Additionally, the over-potential applied also determines the steady-state temperature of the system.

Furthemore, by applying 1% of over-potential above Q_{crit}, the phase change is initiated but is delayed by ~5 seconds before the NDE begins to trigger the thermal runaway (Figure 37d). By stepping to higher over-potentials (i.e., +5%), this delay can be reduced to the same characteristic switching time (~1 second) to improve switching performance.

Understanding the dynamics of this behavior is important for thermal systems where radiative transfer is a dominant mechanism for heat exchange with the environment and IMT materials are of interest for devices such as such as microbolometers[103], [104], heat flux calorimeters[105], space applications[106], etc. Furthermore, a thermal detector could benefit from this characteristic sensitivity to small incremental fluxes near the CHF in order to resolve small power signals. Whereas a 1 nW change in heat input raises the temperature by ~1°C of a 1 mm^2 isolated thin structure discussed above, a 1 nW additional flux near the CHF may trigger a thermal runaway and a larger change in temperature (~35°C). This behavior could be easily detected by a VO_2 based microbolometer carefully designed to operate near CHF. Further studies are necessary to explore the feasibility of this detection scenario and to minimize the thermal mass of the detector for improved detection speeds near CHF.

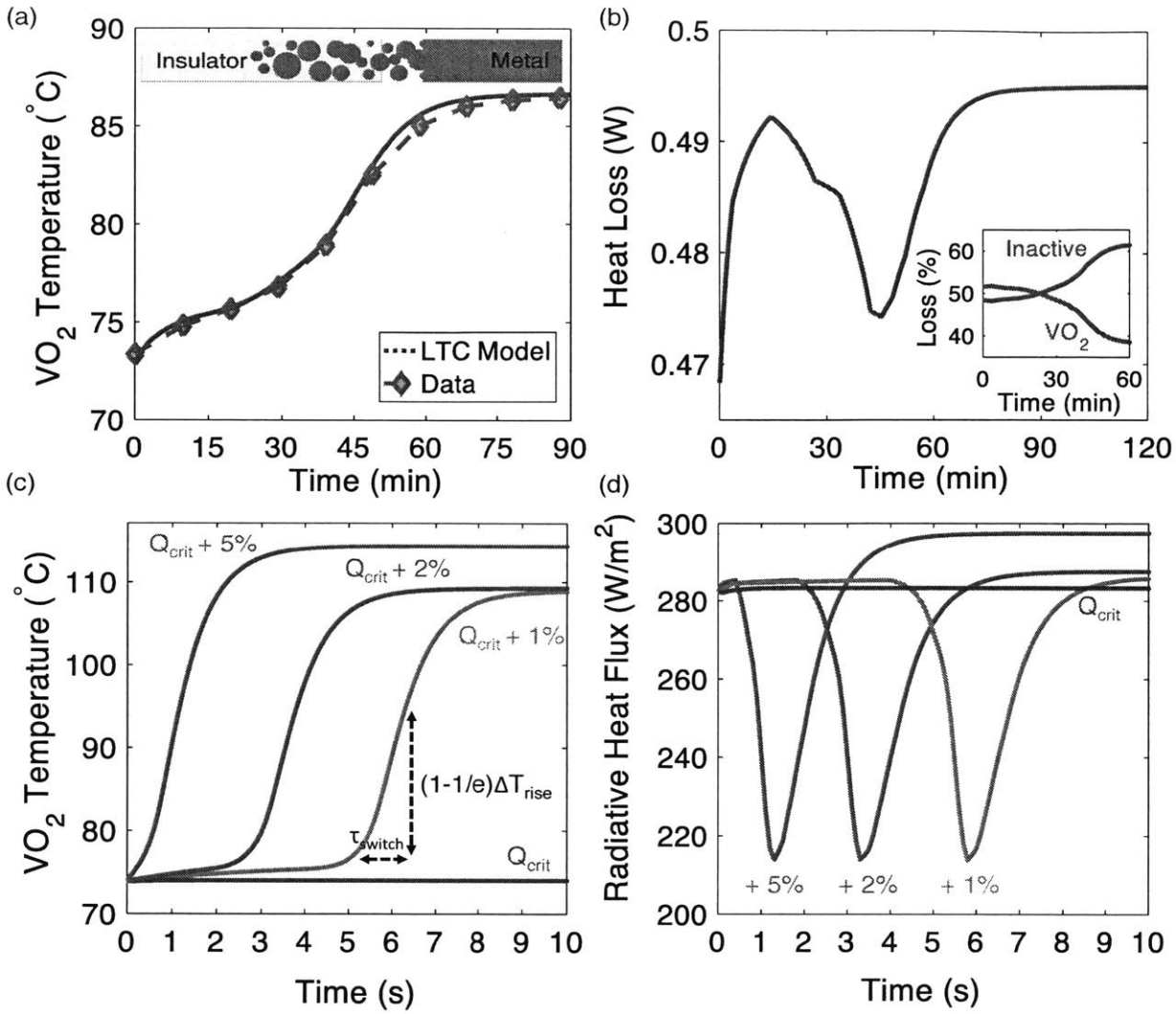

Figure 37: (a) Time-response of a lumped thermal capacitance with a temperature dependent emittance value that represents the percolation of the metallic phase. Experimental data is overlaid to show agreement. (b) Modeled transient heat loss from the device, showing direct evidence that NDE drives thermal runaway. Inset: Percentage of heat loss from both the VO_2 and inactive surface areas. (c) Minimum thermal mass device which shows the limits and tunability of this thermal runaway. With no over-potential above Q''_{crit}, the system equilibrates at 74°C. By applying higher heat fluxes past this point, the onset of NDE can be modified. (d) The corresponding radiative heat flux from the minimum thermal mass device which gives rise to the runaway.

5.5 CONCLUSIONS

While the widespread phenomenon of thermal runaway is often associated with catastrophic failure mechanisms, detailed understanding and control of thermal runaway can give rise to new and important applications, such as in infrared sensing [103], [104], camouflage [8], rectification[107], [108], etc. The temperature sensitivity of the thermal emittance is the critical material property which enables this phenomenon, and the required criteria have been discussed. We have shown direct evidence of NDE in a thermal radiation system through an ultra-thin film of VO_2 and demonstrated how this property gives rise to an uncontrolled thermal runaway. The nature of this thermal runaway is related to both the optical properties of the radiator as well as the thermal mass of the system, leading to a high level of tunability and control of this thermal radiation phenomenon.

Chapter 6

6. Conclusions and Outlooks

6.1 THESIS CONTRIBUTIONS

In this thesis, we broadly explored the potential for solid-state devices which take advantage of spectral and temperature dependent radiative characteristics to enable new capabilities in energy conversion. In chapter 2, we developed a ~4 cm^2 STPV converter which established the current world record for solar-to-electric conversion rates using a high solar concentration, one-dimensional nanostructured selective emitter, and a tandem interference / plasma optical filter. This device demonstrated that an intermediate spectral conversion process wherein the incident solar spectrum is transformed to a tailored thermal emission spectrum could improve the overall device conversion efficiency of the system. These system-level demonstrations were enabled by two main improvements from our previous work: 1) increasing the device footprint by a factor of 4, and 2) targeting the high emission of the Si/SiO_2 material set by incorporating high long-wavelength reflection with a plasma filter.

Chapter 3 analyzed the gap between our STPV demonstration and the potential of this technology. Several different aspects were discussed, but a few critical improvements were identified. Specifically, the photo-thermal efficiency can be vastly improved through the incorporation of a cavity absorber. This allows for a dramatic de-coupling between the absorber and emitter surface areas which shifts the energy balance towards more favorable operation. Additionally, emitter spectral losses and PV non-radiative recombination rates were discussed. We identified a roadmap that shows a practical efficiency limit for STPVs of ~60% solar-to-electrical, ultimately limited by PV cell recombination.

Chapter 4 developed a framework to understand a hybrid solar PV / solar thermal system to maximize exergy generation. The analysis first explored effect of above-gap bandwidth of a hypothetical optical filter. In this work, we identified that an optimum bandwidth exists and it corresponds to the theoretical conversion limit for a given bandgap and absorber temperature. This conclusion was validated using entropic arguments to show that the maximum efficiency corresponds to the system's minimum entropy generation. This analysis provides a framework for researchers interested in developing advanced optical filters for hybrid solar PV / thermal applications.

Chapter 5 discussed an experimental study which explored the phase-transition of vanadium oxide insulator to metal. We used this thermally induced transition to demonstrate broadband negative differential emission for the first time. This phenomenon was exploited to explore the system dynamics of a thermal runaway which is a direct result of the phase transition.

6.2 CHALLENGES FACED

Carrying out the work explained in this thesis was met with many challenges. While annoyances can hinder day-to-day progress, more fundamental drawbacks were encountered and had to be thoughtfully addressed.

Repeatable test platform:
When characterizing device conversion efficiency of a STPV converter, many things can and will go wrong. While phenomena such as misalignment, thermal expansion, melting, degradation, etc. will degrade system performance, in fact the biggest challenge they introduce is impedance to repeatability. The ability for us to characterize our system identically for many runs was paramount. Particularly, it allowed us to use a physics-based model to describe the energy conversion steps. We went through countless iterations of different ideas to ensure repeatability of our STPV tests (of which there were over 150!). Key developments were the use of hypodermic needles and ceramic micro-spheres to isolate the high temperature absorber / emitter element.

Optical power input:
A serious challenge we came across when scaling up our STPV converter was heating it up. Though we were using one of the highest power solar simulators on the market, after two stages of optical concentration, we struggled heating the device up past ~800 deg. C, still ~300 deg. C shy of the optimal operating temperature. To boost the temperature, we had to couple a white-light source into the solar simulator beam using a complicated optical setup. This was not ideal but pushed our device to higher thermal-to-electrical efficiencies. Eventually, we decided that since we were taking advantage of blackbody absorbers, the spectral distribution of the incident light source was unimportant. We determined that high-powered laser diodes were the most straightforward and non-intrusive way to heat our device sufficiently. Extreme caution must be taken when handling laser sources.

Material properties at high temperatures:

When modeling our experimental efforts, we were challenged by understanding how material properties would change at high temperatures. This is an important challenge to address since most properties (particularly optical properties) can change dramatically over such a large temperature difference. High temperature FTIR measurements were made on the Si/SiO_2 photonic crystal which matched our experimental demonstrations very well. Additionally, literature values for hemispherical emittance for evaporated W (used to coat our inactive absorber surface) and thermal conductivity of stainless steel (used to support our materials) were used in our modeling efforts.

6.3 FUTURE DIRECTIONS

The importance of solid-state energy conversion devices should not be overlooked. Developing heat engines which are powered by the sun and contain no moving parts beyond optical concentration can play a vital role for future solar applications. The contributions from the work which is detailed in this thesis help to move the field of STPVs towards real-world applications, but plenty of work remains:

Incorporating Thermal Energy Storage: STPVs will likely never compete with solar PVs. At the end of the day, whether an energy technology will make an impact will come down to the cost per good. One day, STPVs will reach their practical conversion limit (~60% solar to electrical). Solar PVs today are about 20% efficient and cost ~$0.50/W. This suggests that as an intermittent source, STPVs would need to be <$1.50/W to compete with solar PVs today. While possible from a materials perspective, this is an unlikely outcome. Where STPVs can play an enormous role, however, is through the enabling of baseload power generation through the extraction of heat from a thermal energy storage medium. By generating solar-based electrical power at any hour of the day without a battery, STPVs can offer a levelized cost of electricity (LCOE) which rivals, if not undercuts, solar PVs.

However, the incorporation of thermal energy storage in a STPV converter is not trivial. Open research questions in material science and thermal engineering are: 1) What materials exhibit the cost and heat capacity targets to compete with battery technology? 2) How does one design a STPV system which practically integrates thermal energy storage? 3) How does one stabilize the interface shared by a thermal energy storage medium and a thermophotovoltaic device?

Low-bandgap PV cell development: Another key challenge that has yet to be fully addressed is the scalability of various TPV semiconductor materials. Fabricators of such materials (i.e., III-V compounds,

Germanium, etc.) are rare outside of a research setting. This and other recent STPV work plays an important role in opening the eyes of funding agencies that may promote further development of low bandgap materials. Before understanding improving low-bandgap PV performance, perhaps it is more important to understand cost reduction. Strategies to reuse substrates during thin-film III-V compound processing seem like a promising direction for enabling large-area STPV devices.

Component Stability: An often-overlooked challenge in STPV engineering is the stability of components. In this thesis, we explore the conversion of sunlight into electricity using spectral downshifting and spectral splitting. We present a general understanding of the conversion processes but did not explore aspects of durability. Open research questions that can address these issues are: 1) What are the criteria (thermodynamic and kinetic) that ensure selective emitter stability? 2) How does a nanostructured material behave at high temperatures in different environments? 3) What role does emitter evaporation play for long-term power generation?

Ultimately, the success of STPVs will rely on solutions to both technical and economic problems. If the technology is not developed, it cannot be used to help anyone. If there is no one that can be helped, the technology cannot be used to help anyone. It important that as we continue to develop such a converter, we do not lose sight of either perspective.

7. References

[1] "EIA - Annual Energy Outlook 2017." [Online]. Available: https://www.eia.gov/outlooks/aeo/. [Accessed: 18-May-2017].

[2] "What is U.S. electricity generation by energy source? - FAQ - U.S. Energy Information Administration (EIA)." [Online]. Available: https://www.eia.gov/tools/faqs/faq.php?id=427&t=3. [Accessed: 18-May-2017].

[3] "RENEWABLES 2016: GLOBAL STATUS REPORT | Build Up." [Online]. Available: http://www.buildup.eu/en/practices/publications/renewables-2016-global-status-report. [Accessed: 21-May-2017].

[4] MIT Energy Initiative, "The Future of the Electric Grid | MIT Energy Initiative," Cambridge, 2016.

[5] A. Datas, A. Ramos, A. Martí, C. del Cañizo, and A. Luque, "Ultra high temperature latent heat energy storage and thermophotovoltaic energy conversion," *Energy*, vol. 107, pp. 542–549, 2016.

[6] N.-P. Harder and P. Wurfel, "Theoretical limits of thermophotovoltaic solar energy conversion," *Semicond. Sci. Technol.*, vol. 18, no. 5, pp. S151–S157, May 2003.

[7] V. Rinnerbauer *et al.*, "Metallic Photonic Crystal Absorber-Emitter for Efficient Spectral Control in High-Temperature Solar Thermophotovoltaics," *Adv. Energy Mater.*, vol. 4, no. 12, Aug. 2014.

[8] H. Kocer *et al.*, "Thermal tuning of infrared resonant absorbers based on hybrid gold-VO2 nanostructures," *Appl. Phys. Lett.*, vol. 106, no. 16, p. 161104, Apr. 2015.

[9] L. Weinstein, D. Kraemer, K. McEnaney, and G. Chen, "Optical cavity for improved performance of solar receivers in solar-thermal systems," *Sol. Energy*, vol. 108, pp. 69–79, 2014.

[10] A. Lenert *et al.*, "A nanophotonic solar thermophotovoltaic device," *Nat. Nanotechnol.*, vol. 9, no. 2, pp. 126–130, Jan. 2014.

[11] D. M. Bierman, A. Lenert, and E. N. Wang, "Investigation of Design Parameters in Planar Solar Thermophotovoltaic Devices," in *International Heat Transfer Conference 15 - 2014,*

Solar Energy - International Heat Transfer Conference Digital Library, 2014.

[12] V. Siva Reddy, S. C. Kaushik, K. R. Ranjan, and S. K. Tyagi, "State-of-the-art of solar thermal power plants—A review," *Renew. Sustain. Energy Rev.*, vol. 27, pp. 258–273, 2013.

[13] A. Bejan, "Models of power plants that generate minimum entropy while operating at maximum power," *Am. J. Phys.*, vol. 64, no. 8, p. 1054, Aug. 1996.

[14] L. A. Weinstein, J. Loomis, B. Bhatia, D. M. Bierman, E. N. Wang, and G. Chen, "Concentrating Solar Power," *Chem. Rev.*, p. acs.chemrev.5b00397, Oct. 2015.

[15] D. Kraemer *et al.*, "High-performance flat-panel solar thermoelectric generators with high thermal concentration.," *Nat. Mater.*, vol. 10, no. 7, pp. 532–8, Jul. 2011.

[16] G. Segev, Y. Rosenwaks, and A. Kribus, "Limit of efficiency for photon-enhanced thermionic emission vs. photovoltaic and thermal conversion," *Sol. Energy Mater. Sol. Cells*, vol. 140, pp. 464–476, 2015.

[17] W. Shockley and H. J. Queisser, "Detailed Balance Limit of Efficiency of p-n Junction Solar Cells," *J. Appl. Phys.*, vol. 32, no. 3, p. 510, 1961.

[18] C. H. Henry, "Limiting efficiencies of ideal single and multiple energy gap terrestrial solar cells," *J. Appl. Phys.*, vol. 51, no. 8, p. 4494, 1980.

[19] M. A. Green, K. Emery, Y. Hishikawa, and W. Warta, "Solar cell efficiency tables (version 33)," *Prog. Photovoltaics Res. Appl.*, vol. 17, no. 1, pp. 85–94, Jan. 2009.

[20] "Multijunction Solar Cells: Theory and Applications: J.K Rath: 9780750309714: Amazon.com: Books." [Online]. Available: http://www.amazon.com/Multijunction-Solar-Cells-Theory-Applications/dp/0750309717. [Accessed: 10-Apr-2015].

[21] R. J. Ellingson *et al.*, "Highly efficient multiple exciton generation in colloidal PbSe and PbS quantum dots.," *Nano Lett.*, vol. 5, no. 5, pp. 865–71, May 2005.

[22] S. Fan, "Photovoltaics: an alternative 'Sun' for solar cells.," *Nat. Nanotechnol.*, vol. 9, no. 2, pp. 92–3, Feb. 2014.

[23] R. T. Wegh, "Visible Quantum Cutting in LiGdF4:Eu3+ Through Downconversion," *Science (80-.).*, vol. 283, no. 5402, pp. 663–666, Jan. 1999.

[24] T. Trupke, M. A. Green, and P. Würfel, "Improving solar cell efficiencies by down-conversion of high-energy photons," *J. Appl. Phys.*, vol. 92, no. 3, p. 1668, 2002.

[25] A. Shalav, B. S. Richards, and M. A. Green, "Luminescent layers for enhanced silicon solar

cell performance: Up-conversion," *Sol. Energy Mater. Sol. Cells*, vol. 91, no. 9, pp. 829–842, May 2007.

[26] B. S. Richards, "Luminescent layers for enhanced silicon solar cell performance: Down-conversion," *Sol. Energy Mater. Sol. Cells*, vol. 90, no. 9, pp. 1189–1207, May 2006.

[27] A. Manor, L. Martin, and C. Rotschild, "Conservation of photon rate in endothermic photoluminescence and its transition to thermal emission," *Optica*, vol. 2, no. 6, p. 585, Jun. 2015.

[28] H.-Q. Wang, M. Batentschuk, A. Osvet, L. Pinna, and C. J. Brabec, "Rare-Earth Ion Doped Up-Conversion Materials for Photovoltaic Applications," *Adv. Mater.*, vol. 23, no. 22–23, pp. 2675–2680, Jun. 2011.

[29] T. Fix, H. Rinnert, M. G. Blamire, A. Slaoui, and J. L. MacManus-Driscoll, "Nd:SrTiO3 thin films as photon downshifting layers for photovoltaics," *Sol. Energy Mater. Sol. Cells*, vol. 102, pp. 71–74, Jul. 2012.

[30] A. Boccolini, J. Marques-Hueso, D. Chen, Y. Wang, and B. S. Richards, "Physical performance limitations of luminescent down-conversion layers for photovoltaic applications," *Sol. Energy Mater. Sol. Cells*, vol. 122, pp. 8–14, Mar. 2014.

[31] W. G. J. H. M. van Sark, A. Meijerink, R. E. I. Schropp, J. A. M. van Roosmalen, and E. H. Lysen, "Enhancing solar cell efficiency by using spectral converters," *Sol. Energy Mater. Sol. Cells*, vol. 87, no. 1–4, pp. 395–409, May 2005.

[32] W. G. J. H. M. van Sark, "Enhancement of solar cell performance by employing planar spectral converters," *Appl. Phys. Lett.*, vol. 87, no. 15, p. 151117, Oct. 2005.

[33] J. Liu, Q. Yao, and Y. Li, "Effects of downconversion luminescent film in dye-sensitized solar cells," *Appl. Phys. Lett.*, vol. 88, no. 17, p. 173119, Apr. 2006.

[34] S. Ye *et al.*, "Energy transfer between silicon–oxygen-related defects and Yb[sup 3+] in transparent glass ceramics containing Ba[sub 2]TiSi[sub 2]O[sub 8] nanocrystals," *Appl. Phys. Lett.*, vol. 93, no. 18, p. 181110, Nov. 2008.

[35] H.-Q. Wang, M. Batentschuk, A. Osvet, L. Pinna, and C. J. Brabec, "Rare-Earth Ion Doped Up-Conversion Materials for Photovoltaic Applications," *Adv. Mater.*, vol. 23, no. 22–23, pp. 2675–2680, Jun. 2011.

[36] W. R. Chan *et al.*, "Toward high-energy-density, high-efficiency, and moderate-temperature chip-scale thermophotovoltaics.," *Proc. Natl. Acad. Sci. U. S. A.*, vol. 110, no.

14, pp. 5309–14, Apr. 2013.

[37] A. Datas, D. L. Chubb, and A. Veeraragavan, "Steady state analysis of a storage integrated solar thermophotovoltaic (SISTPV) system," *Sol. Energy*, vol. 96, pp. 33–45, Oct. 2013.

[38] M. W. Dashiell *et al.*, "Quaternary InGaAsSb Thermophotovoltaic Diodes," *IEEE Trans. Electron Devices*, vol. 53, no. 12, pp. 2879–2891, Dec. 2006.

[39] V. Stelmakh *et al.*, "Performance of tantalum-tungsten alloy selective emitters in thermophotovoltaic systems," in *SPIE Sensing Technology + Applications*, 2014, p. 911504.

[40] V. Rinnerbauer *et al.*, "High-temperature stability and selective thermal emission of polycrystalline tantalum photonic crystals.," *Opt. Express*, vol. 21, no. 9, pp. 11482–91, May 2013.

[41] Z. Wang *et al.*, "Tunneling-enabled spectrally selective thermal emitter based on flat metallic films," *Appl. Phys. Lett.*, vol. 106, no. 10, p. 101104, Mar. 2015.

[42] W. Li *et al.*, "Plasmonics: Refractory Plasmonics with Titanium Nitride: Broadband Metamaterial Absorber (Adv. Mater. 47/2014)," *Adv. Mater.*, vol. 26, no. 47, pp. 7921–7921, Dec. 2014.

[43] C. Ungaro, S. K. Gray, and M. C. Gupta, "Solar thermophotovoltaic system using nanostructures," *Opt. Express*, vol. 23, no. 19, p. A1149, Aug. 2015.

[44] M. Shimizu, A. Kohiyama, and H. Yugami, "High-efficiency solar-thermophotovoltaic system equipped with a monolithic planar selective absorber/emitter," *J. Photonics Energy*, vol. 5, no. 1, p. 53099, Jan. 2015.

[45] M. Shimizu, A. Kohiyama, and H. Yugami, "10% efficiency solar thermophotovoltaic systems using spectrally controlled monolithic planar absorber/emitters," in *SPIE Photonics Europe*, 2014, p. 91400P.

[46] V. Rinnerbauer *et al.*, "Large-area fabrication of high aspect ratio tantalum photonic crystals for high-temperature selective emitters," *J. Vac. Sci. Technol. B Microelectron. Nanom. Struct.*, vol. 31, no. 1, p. 11802, Dec. 2013.

[47] U. Ortabasi, "Rugate Technology For Thermophotovoltaic (TPV) Applications: A New Approach To Near Perfect Filter Performance," in *AIP Conference Proceedings*, 2003, vol. 653, no. 1, pp. 249–258.

[48] A. Lenert *et al.*, "Addendum: A nanophotonic solar thermophotovoltaic device.," *Nat.*

Nanotechnol., vol. 10, no. 6, p. 563, Jun. 2015.

[49] D. Chubb, *Fundamentals of Thermophotovoltaic Energy Conversion*, 1st ed. Amsterdam: Elsevier B.V., 2007.

[50] T. J. Coutts and J. S. Ward, "Thermophotovoltaic and photovoltaic conversion at high-flux densities," *IEEE Trans. Electron Devices*, vol. 46, no. 10, pp. 2145–2153, 1999.

[51] A. Lenert, Y. Nam, D. M. Bierman, and E. N. Wang, "Role of spectral non-idealities in the design of solar thermophotovoltaics.," *Opt. Express*, vol. 22 Suppl 6, no. 106, pp. A1604-18, Oct. 2014.

[52] C. Wu *et al.*, "Metamaterial-based integrated plasmonic absorber/emitter for solar thermo-photovoltaic systems," *J. Opt.*, vol. 14, no. 2, p. 24005, Feb. 2012.

[53] M. Lin, F. Shyu, and R. Chen, "Optical properties of well-aligned multiwalled carbon nanotube bundles," *Phys. Rev. B*, vol. 61, no. 20, pp. 14114–14118, May 2000.

[54] K. Mizuno *et al.*, "A black body absorber from vertically aligned single-walled carbon nanotubes.," *Proc. Natl. Acad. Sci. U. S. A.*, vol. 106, no. 15, pp. 6044–7, Apr. 2009.

[55] Z.-P. Yang, L. Ci, J. A. Bur, S.-Y. Lin, and P. M. Ajayan, "Experimental observation of an extremely dark material made by a low-density nanotube array.," *Nano Lett.*, vol. 8, no. 2, pp. 446–51, Feb. 2008.

[56] T. Rahmlow and J. Lazo-Wasem, "Design considerations and fabrication results for front surface TPV spectral control filters," in *Sixth Conference on Thermophotovoltaic Generation of Electricity*, 2004.

[57] J. J. Wysocki and P. Rappaport, "Effect of Temperature on Photovoltaic Solar Energy Conversion," *J. Appl. Phys.*, vol. 31, no. 3, p. 571, Jun. 1960.

[58] T. Fujii, "PDMS-based microfluidic devices for biomedical applications," *Microelectron. Eng.*, vol. 61–62, pp. 907–914, Jul. 2002.

[59] D. M. Bierman *et al.*, "Enhanced photovoltaic energy conversion using thermally based spectral shaping," *Nat. Energy*, vol. 1, no. 6, p. 16068, May 2016.

[60] P. T. Landsberg and G. Tonge, "Thermodynamic energy conversion efficiencies," *J. Appl. Phys.*, vol. 51, no. 7, p. R1, Jul. 1980.

[61] P. Jurczak, A. Onno, K. Sablon, and H. Liu, "Efficiency of GaInAs thermophotovoltaic cells: the effects of incident radiation, light trapping and recombinations," *Opt. Express*, vol. 23, no. 19, p. A1208, Sep. 2015.

[62] C. Sah, R. Noyce, and W. Shockley, "Carrier Generation and Recombination in P-N Junctions and P-N Junction Characteristics," *Proc. IRE*, vol. 45, no. 9, pp. 1228–1243, Sep. 1957.

[63] G. Fuchs, C. Schiedel, A. Hangleiter, V. Härle, and F. Scholz, "Auger recombination in strained and unstrained InGaAs/InGaAsP multiple quantum-well lasers," *Appl. Phys. Lett.*, vol. 62, no. 4, pp. 396–398, Jan. 1993.

[64] S. Hausser, G. Fuchs, A. Hangleiter, K. Streubel, and W. T. Tsang, "Auger recombination in bulk and quantum well InGaAs," *Appl. Phys. Lett.*, vol. 56, no. 10, pp. 913–915, Mar. 1990.

[65] C. H. Henry, R. A. Logan, F. R. Merritt, and C. G. Bethea, "Radiative and nonradiative lifetimes in n-type and p-type 1.6 μm InGaAs," *Electron. Lett.*, vol. 20, no. 9, p. 358, 1984.

[66] V. Ganapati, T. P. Xiao, and E. Yablonovitch, "Ultra-Efficient Thermophotovoltaics Exploiting Spectral Filtering by the Photovoltaic Band-Edge," Nov. 2016.

[67] A. (Anthony) Krier, *Mid-infrared semiconductor optoelectronics*. Springer, 2006.

[68] R. Beckert, O. V. Sulima, J. A. Cox, A. W. Bett, and M. G. Mauk, "InGaAsSb photovoltaic cells with enhanced open-circuit voltage," *IEE Proc. - Optoelectron.*, vol. 147, no. 3, pp. 199–204, Jun. 2000.

[69] N. Su, P. Fay, S. Sinharoy, D. Forbes, and D. Scheiman, "Characterization and modeling of InGaAs/InAsP thermophotovoltaic converters under high illumination intensities," *J. Appl. Phys.*, vol. 101, no. 6, p. 64511, Mar. 2007.

[70] R. M. Swanson, "A proposed thermophotovoltaic solar energy conversion system," *Proc. IEEE*, vol. 67, no. 3, pp. 446–447, 1979.

[71] A. G. Imenes and D. R. Mills, "Spectral beam splitting technology for increased conversion efficiency in solar concentrating systems: a review," *Sol. Energy Mater. Sol. Cells*, vol. 84, no. 1–4, pp. 19–69, Oct. 2004.

[72] P. Würfel and U. Würfel, *Physics of Solar Cells: From Basic Principles to Advanced Concepts*. John Wiley & Sons, 2009.

[73] T. P. Otanicar, S. Theisen, T. Norman, H. Tyagi, and R. A. Taylor, "Envisioning advanced solar electricity generation: Parametric studies of CPV/T systems with spectral filtering and high temperature PV," *Appl. Energy*, vol. 140, pp. 224–233, Feb. 2015.

[74] M. A. Hamdy, F. Luttmann, and D. Osborn, "Model of a spectrally selective decoupled

photovoltaic/thermal concentrating system," *Appl. Energy*, vol. 30, no. 3, pp. 209–225, Jan. 1988.

[75] A. Mojiri, R. Taylor, E. Thomsen, and G. Rosengarten, "Spectral beam splitting for efficient conversion of solar energy—A review," *Renew. Sustain. Energy Rev.*, vol. 28, pp. 654–663, Dec. 2013.

[76] H. M. Branz, W. Regan, K. J. Gerst, J. B. Borak, and E. A. Santori, "Hybrid solar converters for maximum exergy and inexpensive dispatchable electricity," *Energy Environ. Sci.*, vol. 8, no. 11, pp. 3083–3091, Oct. 2015.

[77] F. Crisostomo, R. A. Taylor, D. Surjadi, A. Mojiri, G. Rosengarten, and E. R. Hawkes, "Spectral splitting strategy and optical model for the development of a concentrating hybrid PV/T collector," *Appl. Energy*, vol. 141, pp. 238–246, Mar. 2015.

[78] S. Wijewardane and Y. Goswami, "Extended exergy concept to facilitate designing and optimization of frequency-dependent direct energy conversion systems," *Appl. Energy*, vol. 134, pp. 204–214, Dec. 2014.

[79] C. E. Byvik, A. M. Buoncristiani, and B. T. Smith, "Thermodynamic limits for solar energy conversion by a quantum-thermal hybrid system," Nov. 1981.

[80] A. F. Haught, "Physics Considerations of Solar Energy Conversion," *J. Sol. Energy Eng.*, vol. 106, no. 1, p. 3, Feb. 1984.

[81] J. A. Duffie and W. A. Beckman, *Solar engineering of thermal processes*. New York, NY: John Willey & Sons, 1980.

[82] L. Moens and D. M. Blake, "Mechanism of Hydrogen Formation in Solar Parabolic Trough Receivers," *J. Sol. Energy Eng.*, vol. 132, no. 3, p. 31006, Aug. 2010.

[83] P. Wurfel *et al.*, "The chemical potential of radiation," *J. Phys*, vol. 15, pp. 3967–3985, 1982.

[84] F. L. Curzon, "Efficiency of a Carnot engine at maximum power output," *Am. J. Phys.*, vol. 43, no. 1, p. 22, Jan. 1975.

[85] M. Morbidelli and A. Varma, "A generalized criterion for parametric sensitivity: Application to thermal explosion theory," *Chem. Eng. Sci.*, vol. 43, no. 1, pp. 91–102, 1988.

[86] J. C. Leung, H. K. Fauske, and H. G. Fisher, "Thermal runaway reactions in a low thermal inertia apparatus," *Thermochim. Acta*, vol. 104, pp. 13–29, 1986.

[87] K. Nomoto, F.-K. Thielemann, and J. C. Wheeler, "Explosive nucleosynthesis and Type I

supernovae," *Astrophys. J.*, vol. 279, p. L23, Apr. 1984.

[88] J. J. Cowan, A. G. W. Cameron, and J. W. Truran, "The thermal runaway r-process," *Astrophys. J.*, vol. 252, p. 348, Jan. 1982.

[89] V. M. Dwyer, A. J. Franklin, and D. S. Campbell, "Thermal failure in semiconductor devices," *Solid. State. Electron.*, vol. 33, no. 5, pp. 553–560, 1990.

[90] C. Popescu, "Selfheating and thermal runaway phenomena in semiconductor devices," *Solid. State. Electron.*, vol. 13, no. 4, pp. 441–450, 1970.

[91] S. G. Kandlikar, "A Theoretical Model to Predict Pool Boiling CHF Incorporating Effects of Contact Angle and Orientation," *J. Heat Transfer*, vol. 123, no. 6, p. 1071, 2001.

[92] T. G. Theofanous, T. N. Dinh, J. P. Tu, and A. T. Dinh, "The boiling crisis phenomenon: Part II: dryout dynamics and burnout," *Exp. Therm. Fluid Sci.*, vol. 26, no. 6, pp. 793–810, 2002.

[93] V. M. Kenkre, L. Skala, M. W. Weiser, and J. D. Katz, "Theory of microwave interactions in ceramic materials: the phenomenon of thermal runaway," *J. Mater. Sci.*, vol. 26, no. 9, pp. 2483–2489, 1991.

[94] G. A. Kriegsmann, "Thermal runaway in microwave heated ceramics: A one-dimensional model," *J. Appl. Phys.*, vol. 71, no. 4, p. 1960, 1992.

[95] P. Friedlingstein *et al.*, "Positive feedback between future climate change and the carbon cycle," *Geophys. Res. Lett.*, vol. 28, no. 8, pp. 1543–1546, Apr. 2001.

[96] M. Imada, A. Fujimori, and Y. Tokura, "Metal-insulator transitions," *Rev. Mod. Phys.*, vol. 70, no. 4, pp. 1039–1263, Oct. 1998.

[97] M. Liu *et al.*, "Terahertz-field-induced insulator-to-metal transition in vanadium dioxide metamaterial," *Nature*, vol. 487, no. 7407, pp. 345–348, Jul. 2012.

[98] A. Zylbersztejn and N. F. Mott, "Metal-insulator transition in vanadium dioxide," *Phys. Rev. B*, vol. 11, no. 11, pp. 4383–4395, Jun. 1975.

[99] J. D. Budai *et al.*, "Metallization of vanadium dioxide driven by large phonon entropy," *Nature*, vol. 515, no. 7528, pp. 535–539, Nov. 2014.

[100] M. M. Qazilbash *et al.*, "Mott Transition in VO2 Revealed by Infrared Spectroscopy and Nano-Imaging," *Science (80-.).*, vol. 318, no. 5857, 2007.

[101] M. A. Kats *et al.*, "Ultra-thin perfect absorber employing a tunable phase change material," *Appl. Phys. Lett.*, vol. 101, no. 22, p. 221101, 2012.

[102] J. Narayan and V. M. Bhosle, "Phase transition and critical issues in structure-property correlations of vanadium oxide," *J. Appl. Phys.*, vol. 100, no. 10, p. 103524, 2006.

[103] C. Chen, X. Yi, J. Zhang, and X. Zhao, "Linear uncooled microbolometer array based on VOx thin films," *Infrared Phys. Technol.*, vol. 42, no. 2, pp. 87–90, 2001.

[104] L. A. L. de Almeida, G. S. Deep, A. M. N. Lima, I. A. Khrebtov, V. G. Malyarov, and H. Neff, "Modeling and performance of vanadium–oxide transition edge microbolometers," *Appl. Phys. Lett.*, vol. 85, no. 16, p. 3605, 2004.

[105] M. C. Wingert, Z. C. Y. Chen, S. Kwon, J. Xiang, and R. Chen, "Ultra-sensitive thermal conductance measurement of one-dimensional nanostructures enhanced by differential bridge," *Rev. Sci. Instrum.*, vol. 83, no. 2, p. 24901, 2012.

[106] A. Ochi *et al.*, "Variable Thermal Emittance Radiator Using Metal-Insulator Phase Transition in $La_{1-x}Sr_xMnO_3$," *Jpn. J. Appl. Phys.*, vol. 41, no. Part 1, No. 11B, pp. 7263–7265, Nov. 2002.

[107] E. Nefzaoui, J. Drevillon, Y. Ezzahri, and K. Joulain, "A simple radiative thermal diode," Jun. 2013.

[108] Y. Yang, S. Basu, and L. Wang, "Radiation-based near-field thermal rectification with phase transition materials," *Appl. Phys. Lett.*, vol. 103, no. 16, p. 163101, 2013.